RESEARCH ARTICLE | MARCH 25 2024

Numerical investigation of flow past a cylinder using cumulant lattice Boltzmann method

Enbo Xing (邢恩博) ; Guangwei Liu (刘光威) ; Qinghe Zhang (张庆河) ; Jinfeng Zhang (张金凤) ; Chaoqun Ji (季超群)

Physics of Fluids 36, 035166 (2024)
https://doi.org/10.1063/5.0195370

Physics of Fluids ARTICLE pubs.aip.org/aip/pof

Numerical investigation of flow past a cylinder using cumulant lattice Boltzmann method

Cite as: Phys. Fluids **36**, 035166 (2024); doi: 10.1063/5.0195370
Submitted: 2 January 2024 · Accepted: 10 March 2024 ·
Published Online: 25 March 2024

Enbo Xing (邢恩博),[1] Guangwei Liu (刘光威),[1,a)] Qinghe Zhang (张庆河),[1] Jinfeng Zhang (张金凤),[1,2] and Chaoqun Ji (季超群)[1]

AFFILIATIONS

[1]State Key Laboratory of Hydraulic Engineering Intelligent Construction and Operation, Tianjin University, Tianjin 300072, China
[2]Key Laboratory of Earthquake Engineering Simulation and Seismic Resilience of China Earthquake Administration, Tianjin University, Tianjin 300350, China

[a)]Author to whom correspondence should be addressed: guangweiliu@tju.edu.cn

ABSTRACT

This paper presents simulations of flow past a circular cylinder within the subcritical Reynolds number (Re) range from 3900 to 2×10^5, utilizing the parameterized cumulant lattice Boltzmann model. In this study, a three-dimensional characteristic boundary condition for incompressible flow has been integrated into the lattice Boltzmann method at the outflow boundary to minimize spurious reflection. The flow field, wake statistics, hydrodynamic force, and power spectra results of $\mathrm{Re} = 3900$ from the cumulant lattice Boltzmann model are exhaustively compared with the laboratory data and other numerical models. Relative to other numerical models employing turbulence closure, the cumulant lattice Boltzmann simulations demonstrate enhanced agreement with the experimental data even with relatively coarser grid resolution. The resolution-spanning feature for the cumulant lattice Boltzmann model in turbulent flows, without using explicit turbulence model, aligns with the previous benchmark case studies. The stability-preserving regularization process in the present model is analyzed. Results indicate that the influence of the regularization parameter is mitigated with improved grid resolution. A specific regularization parameter for flow around cylinder simulations is recommended. Variations in flow properties and hydrodynamic forces within the subcritical Reynolds number range of 3900 to 2×10^5 are analyzed. The results confirm that the parameterized cumulant lattice Boltzmann model can accurately simulate practical engineering flows, characterized by complex separation and recirculation, within the subcritical range. Moreover, the computational efficiency and parallel scalability are compared with other numerical methods.

I. INTRODUCTION

Flow past a circular cylinder is prevalent in offshore engineering, observed commonly around offshore platforms, wind turbine foundations, and marine risers. Flow-induced forces constitute one of primary loads on these structures.[1] Flow separation around these structures often leads to vortex shedding, causing vibrations[2] and local scour.[3] These phenomena pose potential threats to structural safety. Consequently, the knowledge of the flow past a circular cylinder is essential for the design of offshore structures.

Flow regimes of flow past a circular cylinder are categorized into three major groups based on the Reynolds number (Re), as outlined in review papers:[4–8] (i) laminar phase ($\mathrm{Re} < 300$); (ii) subcritical phase ($300 < \mathrm{Re} < 2 \times 10^5$); (iii) critical and supercritical phase ($\mathrm{Re} > 2 \times 10^5$). The flow properties and hydrodynamic forces vary depending on the Reynolds number across the different flow regions. In the subcritical range, numerous wind and water tunnel physical experiments have been conducted, measuring the drag coefficient (C_d), the lift coefficient (C_l), the pressure coefficient (C_p), and the Strouhal number (St).[9–26] Experimental data for validating the numerical model are available in the subcritical range, particularly for the case at $\mathrm{Re} = 3900$. With the advancement of computing power, numerical simulations have gained increased attention for their capability to provide detailed flow field insight. Numerical investigations using various numerical methods, such as the finite difference method (FDM),[24,27,28] finite volume method (FVM),[29–41] and high-order spectral/hp element method (HEM),[30,42–44] have been conducted in the subcritical range. However, with increasing Reynolds number, an exceedingly fine mesh resolution becomes necessary to accurately resolve the three-dimensional (3D) and unsteady flow fields in direct numerical simulation (DNS) and large eddy simulation (LES). This requirement leads to substantial computational costs[30] due to nonlinear parallel scalability challenges,[45] consequently restricting the practical applicability of the conventional numerical models.

Recently, the lattice Boltzmann method (LBM) has gained increasing attention for its excellent parallel scalability on both central processing unit (CPU) and graphics processing unit (GPU) clusters.[45–49] However, the traditional lattice Boltzmann (LB) scheme, employing the BGK collision operator, is hindered by low stability and reduced accuracy at high Reynolds number. This limitation restricts its application in practical engineering flow simulations.[50,51] Accordingly, a series of improvements has been proposed to overcome these drawbacks, like the multi-relaxation-time (MRT) model,[52–54] cascaded model,[55,56] central moments model,[57,58] entropy model,[59,60] and cumulant model.[50,51] Among these improvements, the cumulant LBM demonstrates great potential due to its remarkable stability and enhanced accuracy at high Reynolds number.[47,61–64] The cumulant LBM model was initially proposed by Geier *et al.*[50] Subsequently, the model was further optimized by parameterizing the free relaxation parameters to achieve fourth-order accuracy for the diffusion term and enhanced stability at high Reynolds number through regularization of the third-order cumulants using a regularized parameter named "limiter."[51] Previous simulations using the cumulant model on benchmark cases, including the Taylor-Green vortex, turbulent channel flow, and flow over periodic hill,[50,51,61,65–68] have shown promising predictive performance. Remarkably, these outcomes were achieved with relatively coarser resolution (about $y^+ < 50$) and without requiring an explicit turbulence model.[61,67] This advantage significantly reduces the grid resolution requirement, thereby extending the simulation capabilities of the LBM. Despite its potential, the application of the cumulant LBM model to simulate flow past a circular cylinder remains a relatively unexplored area. This study aims to thoroughly investigate the capability of the parameterized cumulant LBM model in accurately modeling the flow past a circular cylinder in the subcritical range, which is a classic example of practical engineering flow characterized by complex separation and recirculation patterns. The simulation results are meticulously compared with experimental data to validate various aspects, including flow fields, wake statistics, hydrodynamic forces, and power spectra at $\mathrm{Re} = 3900$. Additionally, the grid resolution of our simulations is evaluated against other scale-resolving numerical simulations. The influence of the regularization process and regularization parameter is analyzed, and an appropriate regularization parameter for simulations of flow past a circular cylinder is proposed. Furthermore, variations in flow properties and hydrodynamic forces are investigated in the subcritical range of $\mathrm{Re} = 3900$ to $\mathrm{Re} = 2 \times 10^5$. Both qualitative and quantitative analyses are employed to understand the underlying physical mechanisms of these variations. Discussions on the advantages of the current CLBM model are also included.

This paper is organized as follows: After the Introduction, the details of the cumulant LBM model and boundary conditions are presented in Sec. II. The simulation results of flow past a circular cylinder at $\mathrm{Re} = 3900$ are thoroughly compared with both experimental and other numerical results in Sec. III. Detailed examinations of the regularization process and regularization parameter are also presented in Sec. III. Variations in flow properties and hydrodynamic forces across Re range from 3900 to 2×10^5 are explored in Sec. IV. The computational efficiency and parallel scalability are discussed in Sec. V. Finally, the concluding remarks are presented in Sec. VI.

II. NUMERICAL MODEL

This section briefly introduces the cumulant LB scheme, featuring parameterized and regularized relaxation rates. The derivation of the three-dimensional characteristic outflow boundary condition is presented, along with a summary of other boundary conditions.

A. Parameterized cumulant Lattice Boltzmann method

The lattice Boltzmann equation (LBE) is a numerical approximation of the Boltzmann equation, solved through a set of discrete particle distribution functions (PDFs)

$$f_{ijk}(\mathbf{x} + \mathbf{e}_{ijk}\Delta t, t + \Delta t) = f_{ijk}(\mathbf{x}, t) + \Delta t \Omega_{ijk}, \tag{1}$$

where f_{ijk} denotes the PDF and Ω_{ijk} represents the collision operator. $\mathbf{e}_{ijk}$ corresponds to the discrete velocity matrix

$$\mathbf{e}_{ijk} = c \begin{bmatrix} 0 & 1 & -1 & 0 & 0 & 0 & 0 & 1 & -1 & 1 & -1 & 1 & -1 & 1 & -1 & 0 & 0 & 0 & 0 & 1 & -1 & 1 & -1 & 1 & -1 & -1 & 1 \\ 0 & 0 & 0 & 1 & -1 & 0 & 0 & 1 & 1 & -1 & -1 & 0 & 0 & 0 & 0 & 1 & -1 & 1 & -1 & 1 & -1 & 1 & -1 & -1 & 1 & 1 & -1 \\ 0 & 0 & 0 & 0 & 0 & 1 & -1 & 0 & 0 & 0 & 0 & 1 & 1 & -1 & -1 & 1 & 1 & -1 & -1 & 1 & -1 & 1 & -1 & -1 & 1 & 1 & -1 \end{bmatrix}^T, \tag{2}$$

the lattice speed $c = \Delta x/\Delta t$, where Δx is the lattice length and Δt is the time step. Under the Chapman–Enskog analysis,[69] the LBE converges to the incompressible Navier–Stokes (NS) equations, assuming a small Mach (Ma) number. Macroscopic quantities, such as pressure p and velocity $\mathbf{u} = (u, v, w)$, are obtained from the zero and the first moments of the PDFs

$$p = c_s^2 \sum_{i=-1}^{1} \sum_{j=-1}^{1} \sum_{k=-1}^{1} f_{ijk}, \tag{3}$$

$$\mathbf{u} = \frac{1}{\rho} \sum_{i=-1}^{1} \sum_{j=-1}^{1} \sum_{k=-1}^{1} f_{ijk} \mathbf{e}_{ijk}, \tag{4}$$

where $c_s = c/\sqrt{3}$ is the speed of the sound in the lattice.

The cumulant collision scheme employed in this paper was proposed by Geier *et al.*[51] To conserve space while maintaining completeness, this section focuses on the major implementation aspects of the cumulant collision operator. The derivation of the cumulant scheme and more detail information are referred to the original work by Geier *et al.*[51] The first step is transforming the PDFs from discrete velocity space to the frequency space and calculating the cumulants. However, direct computation of the cumulants is time-consuming. A more straightforward approach is transforming the PDFs f_{ijk} to the central moments $\kappa_{\alpha\beta\gamma}$ initially

$$\kappa_{a\beta\gamma} = \sum_{i,j,k} (i - u/c)^{\alpha} (j - \nu/c)^{\beta} (k - w/c)^{\gamma} f_{ijk}. \tag{5}$$

Subsequently, the cumulants $C_{\alpha\beta\gamma}$ are computed from the central moments $\kappa_{\alpha\beta\gamma}$. Both the zeroth- and the first-order cumulants are

zero. Cumulants from the second to the third order are equal to the corresponding central moments

$$C_{\alpha\beta\gamma} = \kappa_{\alpha\beta\gamma},\ \alpha+\beta+\gamma = 2, 3. \tag{6}$$

Cumulants from the fourth to the sixth order are

$$C_{211} = \kappa_{211} - ((\kappa_{200} + 1/3)\kappa_{011} + 2\kappa_{110}\kappa_{101})/\rho, \tag{7}$$

$$C_{220} = \kappa_{220} - \left(\left(\left(\kappa_{200}\kappa_{020} + 2\kappa_{110}^2\right) + (\kappa_{200} + \kappa_{020})/3\right)/\rho - (\delta\rho/\rho)/9\right), \tag{8}$$

$$\begin{aligned} C_{122} = \kappa_{122} - ((&\kappa_{002}\kappa_{120} + \kappa_{020}\kappa_{102} + 4\kappa_{011}\kappa_{111} \\ &+2(\kappa_{101}\kappa_{021} + \kappa_{110}\kappa_{012})) + (\kappa_{120} + \kappa_{102})/3)/\rho, \end{aligned} \tag{9}$$

$$\begin{aligned} C_{222} = \kappa_{222} - &\left(4\kappa_{111}^2 + \kappa_{200}\kappa_{022} + \kappa_{020}\kappa_{202} + \kappa_{002}\kappa_{220}\right. \\ &+ 4(\kappa_{011}\kappa_{211} + \kappa_{101}\kappa_{121} + \kappa_{110}\kappa_{112}) \\ &+ 2(\kappa_{120}\kappa_{102} + \kappa_{210}\kappa_{012} + \kappa_{201}\kappa_{021}))/\rho \\ &+ \left(16\kappa_{110}\kappa_{101}\kappa_{011} + 4\left(\kappa_{101}^2\kappa_{020} + \kappa_{011}^2\kappa_{200} + \kappa_{110}^2\kappa_{002}\right)\right. \\ &+2\kappa_{200}\kappa_{020}\kappa_{002})/\rho^2 - (3(\kappa_{022} + \kappa_{202} + \kappa_{220}) \\ &+(\kappa_{200} + \kappa_{020} + \kappa_{002}))/(9\rho) + 2\left(2\left(\kappa_{101}^2 + \kappa_{011}^2 + \kappa_{110}^2\right)\right. \\ &+ (\kappa_{002}\kappa_{020} + \kappa_{002}\kappa_{200} + \kappa_{020}\kappa_{200}) \\ &+(\kappa_{002} + \kappa_{020} + \kappa_{200})/3\left.\right)/\left(3\rho^2\right) \\ &+ \left(\delta\rho^2 - \delta\rho\right)/\left(27\rho^2\right), \end{aligned} \tag{10}$$

and cumulants not presented here can be derived by permuting the subscript indices.

Once the cumulants have been calculated, the collision process is explicitly conducted in the cumulant space, and the post-collision cumulants $C^*_{\alpha\beta\gamma}$ are calculated as $C^*_{\alpha\beta\gamma} = (1 - \omega_{\alpha\beta\gamma})C_{\alpha\beta\gamma}$ expect for the following post-collision cumulants

$$\begin{aligned} C^*_{200} - C^*_{020} = (1-\omega_1)(C_{200} - C_{020}) \\ - 3\rho\left(1 - \frac{\omega_1}{2}\right)\left(u^2 D_x u - v^2 D_y v\right), \end{aligned} \tag{11}$$

$$\begin{aligned} C^*_{200} - C^*_{002} = (1-\omega_1)(C_{200} - C_{002}) \\ - 3\rho\left(1 - \frac{\omega_1}{2}\right)\left(u^2 D_x u - w^2 D_z w\right), \end{aligned} \tag{12}$$

$$\begin{aligned} C^*_{200} + C^*_{020} + C^*_{002} = \kappa_{000}\omega_2 + (1-\omega_2)(C_{200} + C_{020} + C_{002}) \\ - 3\rho\left(1 - \frac{\omega_2}{2}\right)\left(u^2 D_x u + v^2 D_y v + w^2 D_z w\right), \end{aligned} \tag{13}$$

$$C^*_{120} + C^*_{102} = \left(1 - \omega^L_{3,1}\right)(C_{120} + C_{102}), \tag{14}$$

$$C^*_{210} + C^*_{012} = \left(1 - \omega^L_{3,2}\right)(C_{210} + C_{012}), \tag{15}$$

$$C^*_{201} + C^*_{021} = \left(1 - \omega^L_{3,3}\right)(C_{201} + C_{021}), \tag{16}$$

$$C^*_{120} - C^*_{102} = \left(1 - \omega^L_{4,1}\right)(C_{120} - C_{102}), \tag{17}$$

$$C^*_{210} - C^*_{012} = \left(1 - \omega^L_{4,2}\right)(C_{210} - C_{012}), \tag{18}$$

$$C^*_{201} - C^*_{021} = \left(1 - \omega^L_{4,3}\right)(C_{201} - C_{021}), \tag{19}$$

$$C^*_{111} = \left(1 - \omega^L_5\right)C_{111}, \tag{20}$$

$$\begin{aligned} C^*_{220} - 2C^*_{202} + C^*_{022} = \frac{2}{3}\left(\frac{1}{\omega_1} - \frac{1}{2}\right)\omega_6 A\rho(D_x u - 2D_y v + D_z w) \\ + (1-\omega_6)(C_{220} - 2C_{202} + C_{022}), \end{aligned} \tag{21}$$

$$\begin{aligned} C^*_{220} + C^*_{202} - 2C^*_{022} = \frac{2}{3}\left(\frac{1}{\omega_1} - \frac{1}{2}\right)\omega_6 A\rho(D_x u + D_y v - 2D_z w) \\ + (1-\omega_6)(C_{220} + C_{202} - 2C_{022}), \end{aligned} \tag{22}$$

$$\begin{aligned} C^*_{220} + C^*_{202} + C^*_{022} = -\frac{4}{3}\left(\frac{1}{\omega_1} - \frac{1}{2}\right)\omega_7 A\rho(D_x u + D_y v + D_z w) \\ + (1-\omega_7)(C_{220} + C_{202} + C_{022}), \end{aligned} \tag{23}$$

$$C^*_{211} = -\frac{1}{3}\left(\frac{1}{\omega_1} - \frac{1}{2}\right)\omega_8 B\rho(D_y w + D_z v) + (1-\omega_8)C_{211}, \tag{24}$$

$$C^*_{121} = -\frac{1}{3}\left(\frac{1}{\omega_1} - \frac{1}{2}\right)\omega_8 B\rho(D_x w + D_z u) + (1-\omega_8)C_{121}, \tag{25}$$

$$C^*_{112} = -\frac{1}{3}\left(\frac{1}{\omega_1} - \frac{1}{2}\right)\omega_8 B\rho(D_x v + D_y u) + (1-\omega_8)C_{112}. \tag{26}$$

Apart from the basic collision procedure, three significant modifications have been incorporated. The first modification involves using the derivatives of velocity in the collision of the second-order cumulants, as shown in Eqs. (11)–(13), effectively removing the spurious dependency of the viscosity on the velocity in other LB schemes. The velocity gradient can be represented by the second-order cumulants:

$$\begin{aligned} D_x u = -\frac{\omega_1}{2\rho}(2C_{200} - C_{020} - C_{002}) \\ -\frac{\omega_2}{2\rho}(C_{200} + C_{020} + C_{002} - \kappa_{000}), \end{aligned} \tag{27}$$

$$D_y v = D_x u + \frac{3\omega_1}{2\rho}(C_{200} - C_{020}), \tag{28}$$

$$D_z w = D_x u + \frac{3\omega_1}{2\rho}(C_{200} - C_{002}), \tag{29}$$

$$D_x v + D_y u = -\frac{3\omega_1}{\rho}C_{110}, \tag{30}$$

$$D_x w + D_z u = -\frac{3\omega_1}{\rho}C_{101}, \tag{31}$$

$$D_y w + D_z v = -\frac{3\omega_1}{\rho}C_{011}. \tag{32}$$

Then, by optimizing the leading error of the collision operator, the parameterized relaxation rates $\omega_3, \omega_4, \omega_5$ and two additional parameters A, B are utilized in Eqs. (14)–(26) to achieve fourth-order accuracy of the diffusion term

$$\omega_3 = \frac{8\left(2\omega_1^2 - 3\omega_1 - 2\right)}{7\omega_1^2 - 14\omega_1 - 8}, \tag{33}$$

$$\omega_4 = \frac{8\left(4\omega_1^2 - 15\omega_1 + 14\right)}{9\omega_1^2 - 50\omega_1 + 56}, \tag{34}$$

$$\omega_5 = \frac{24\left(3\omega_1^3 - 13\omega_1^2 + 12\omega_1 + 4\right)}{29\omega_1^3 - 130\omega_1^2 + 152\omega_1 + 48}, \tag{35}$$

$$A = \frac{-3\omega_1^2 + 2\omega_1 + 4}{5\omega_1^2 - 7\omega_1 + 2}, \tag{36}$$

$$B = \frac{-14\omega_1^2 + 28\omega_1 + 4}{15\omega_1^2 - 21\omega_1 + 6}. \tag{37}$$

The fluid kinematic viscosity related relaxation rates ω_1 is calculated as follows:

$$\omega_1 = \frac{1}{\nu/c_s^2 + \Delta t/2}. \tag{38}$$

The bulk viscosity related relaxation rate ω_2 and high-order relaxation rates $\omega_6 \sim \omega_{10}$ are set to one in this study.

Owing to the numerical instability caused by parameterized relaxation rates $\omega_3, \omega_4, \omega_5 \to 0$ under the low viscosity conditions, the last modification is regularizing the relaxation rates in Eqs. (14)–(20) by a regularization parameter named as limiter. The regularized relaxation rates are defined as follows:

$$\omega_{3,1}^L = \omega_3 + \frac{(1-\omega_3)|C_{120} + C_{102}|}{\rho\lambda + |C_{120} + C_{102}|}, \tag{39}$$

$$\omega_{3,2}^L = \omega_3 + \frac{(1-\omega_3)|C_{210} + C_{012}|}{\rho\lambda + |C_{210} + C_{012}|}, \tag{40}$$

$$\omega_{3,3}^L = \omega_3 + \frac{(1-\omega_3)|C_{201} + C_{021}|}{\rho\lambda + |C_{201} + C_{021}|}, \tag{41}$$

$$\omega_{4,1}^L = \omega_4 + \frac{(1-\omega_4)|C_{120} - C_{102}|}{\rho\lambda + |C_{120} - C_{102}|}, \tag{42}$$

$$\omega_{4,2}^L = \omega_4 + \frac{(1-\omega_4)|C_{210} - C_{012}|}{\rho\lambda + |C_{210} - C_{012}|}, \tag{43}$$

$$\omega_{4,3}^L = \omega_4 + \frac{(1-\omega_4)|C_{201} - C_{021}|}{\rho\lambda + |C_{201} - C_{021}|}, \tag{44}$$

$$\omega_5^L = \omega_5 + \frac{(1-\omega_5)|C_{111}|}{\rho\lambda + |C_{111}|}, \tag{45}$$

where limiter λ is an adjustable parameter, with a default value of 0.01 as suggested by Geier *et al.*[51] In subsequent studies, Gehrke and Rung[68] recommended adjusting the regularization parameter value between 0.1 and 1, based on a series of periodic hill flow simulations. Subsequently, they further assumed a relationship between the grid resolution and the regularization parameter.[67]

After the collision, the post-collision cumulants $C^*_{\alpha\beta\gamma}$ are transformed back into the post-collision central moments $\kappa^*_{\alpha\beta\gamma}$, and then into the post-collision PDFs f^*_{ijk}. These steps are the inverse of the forward transformation outlined in Eqs. (6)–(10) and Eq. (5). For brevity, these procedures are omitted, and the detailed formulations are available in work by Geier *et al.*[51] Then, the post-collision PDFs stream to the neighboring grids as

$$f_{ijk}(\mathbf{x} + \mathbf{e}_{ijk}\Delta t, t + \Delta t) = f^*_{ijk}(\mathbf{x}, t) \tag{46}$$

completing the entire process of the cumulant LB scheme within a single time step.

B. Boundary conditions

1. Open boundary

Owing to the weakly compressible nature of the LBM, pressure waves within the simulation domain propagate at the sound speed c_s and are consequently reflected at the boundaries. Such reflections can lead to spurious pressure reflections and steep velocity gradients, ultimately leading to the breakdown of the simulation. It has been demonstrated that the characteristic boundary condition (CBC) effectively removes spurious reflections at the open boundary in 2D LBM simulations.[70] Thus, this study extends the CBC method to 3D incompressible LBM simulations.

The CBC solves a set of simplified NS equations without transverse and viscous terms, known as local one-dimensional inviscid (LODI) equations, at the boundary. For a 3D outflow open boundary normal to the x-direction, the LODI equations corresponding to the macroscopic governing equations of the incompressible LB scheme[69] are written as follows:

$$\frac{1}{\rho_0}\frac{\partial \rho}{\partial t} + \frac{\partial u_x}{\partial x} = 0, \tag{47}$$

$$\frac{\partial u_x}{\partial t} + u_x\frac{\partial u_x}{\partial x} + \frac{1}{\rho_0}\frac{\partial p}{\partial x} = 0, \tag{48}$$

$$\frac{\partial u_y}{\partial t} + u_x\frac{\partial u_y}{\partial x} = 0, \tag{49}$$

$$\frac{\partial u_z}{\partial t} + u_z\frac{\partial u_z}{\partial x} = 0. \tag{50}$$

As suggested by Schlaffer[71] for deriving 2D incompressible CBC, an additional term $\frac{u_x}{\rho_0}\frac{\partial \rho}{\partial x}$ is added in the continuity equation. Also, with the relationship between pressure and density $p = \rho c_s^2$ in the LB scheme, the continuity equation is changed as follows:

$$\frac{\partial p}{\partial t} + u_x\frac{\partial p}{\partial x} + \rho_0 c_s^2\frac{\partial u_x}{\partial x} = 0. \tag{51}$$

Consequently, the LODI equations are Eqs. (48)–(51). The energy equation is omitted in this context, as the employed LB scheme is athermal.[72] Then, the LODI equations are expressed in the vector form:

$$\frac{\partial \mathbf{U}}{\partial t} + \mathbf{A}\frac{\partial \mathbf{U}}{\partial x} = 0, \tag{52}$$

where $\mathbf{U} = (p, u_x, u_y, u_z)$ and $\mathbf{A}$ is the parameter matrix

$$\mathbf{A} = \begin{pmatrix} u_x & \rho_0 c_s^2 & 0 & 0 \\ \frac{1}{\rho_0} & u_x & 0 & 0 \\ 0 & 0 & u_x & 0 \\ 0 & 0 & 0 & u_x \end{pmatrix}. \tag{53}$$

Utilizing eigenvector decomposition, the parameter matrix is decomposed into $\mathbf{SAS}^{-1} = \mathbf{\Lambda}$, where $\mathbf{\Lambda}$ is the diagonal matrix of the eigenvalues and $\mathbf{S}$ is the matrix of eigenvectors. They are given as follows:

$$\mathbf{\Lambda} = \mathrm{diag}(\lambda_1, \lambda_2, \lambda_3, \lambda_4) = \mathrm{diag}(u_x, u_x, u_x + c_s, u_x - c_x), \tag{54}$$

$$\mathbf{S} = \begin{pmatrix} 0 & 0 & 0 & 1 \\ 0 & 0 & 1 & 0 \\ \frac{1}{2c_s\rho_0} & \frac{1}{2} & 0 & 0 \\ -\frac{1}{2c_s\rho_0} & \frac{1}{2} & 0 & 0 \end{pmatrix}, \tag{55}$$

where λ_i is the characteristic velocities at the boundary. The directions of the characteristic velocities are illustrated in Fig. 1. The corresponding wave amplitude $\mathbf{L}$ is computed as follows:

$$\mathbf{L} = \mathbf{\Lambda S}\frac{\partial \mathbf{U}}{\partial x} = \begin{pmatrix} L_1 \\ L_2 \\ L_3 \\ L_4 \end{pmatrix} = \begin{pmatrix} u_x \dfrac{\partial u_z}{\partial x} \\ u_x \dfrac{\partial u_y}{\partial x} \\ (u_x + c_s)\left(\dfrac{1}{2c_s\rho_0}\dfrac{\partial p}{\partial x} + \dfrac{1}{2}\dfrac{\partial u_x}{\partial x}\right) \\ (u_x - c_s)\left(-\dfrac{1}{2c_s\rho_0}\dfrac{\partial p}{\partial x} + \dfrac{1}{2}\dfrac{\partial u_x}{\partial x}\right) \end{pmatrix}. \tag{56}$$

Subsequently, by applying Eq. (56), the LODI equations $\frac{\partial \mathbf{U}}{\partial t} + \mathbf{S}^{-1}\mathbf{L} = 0$ are transformed to

$$\frac{\partial p}{\partial t} + \rho_0 c_s(L_3 - L_4) = 0, \tag{57}$$

$$\frac{\partial u_x}{\partial t} + (L_3 + L_4) = 0, \tag{58}$$

$$\frac{\partial u_y}{\partial t} + L_2 = 0, \tag{59}$$

$$\frac{\partial u_z}{\partial t} + L_3 = 0. \tag{60}$$

At the outlet open boundary condition on the right side, a non-reflective boundary condition is achieved by setting the characteristic wave amplitude of the incident wave (L_4) to zero. By substituting Eq. (56) into Eqs. (57)–(60) and applying the first-order time forward scheme, the unknown macroscopic quantities are calculated as follows:

$$p^t = p^{t-1} - \delta t\left(u_x^{t-1} + c_s\right)\left(\frac{1}{2}\frac{\partial p^{t-1}}{\partial x} + \frac{\rho_0 c_s}{2}\frac{\partial u_x^{t-1}}{\partial x}\right), \tag{61}$$

$$u_x^t = u_x^{t-1} - \delta t\left(u_x^{t-1} + c_s\right)\left(\frac{1}{2\rho_0 c_s}\frac{\partial p^{t-1}}{\partial x} + \frac{1}{2}\frac{\partial u_x^{t-1}}{\partial x}\right), \tag{62}$$

$$u_y^t = u_y^{t-1} - \delta t u_x^{t-1}\frac{\partial u_y^{t-1}}{\partial x}, \tag{63}$$

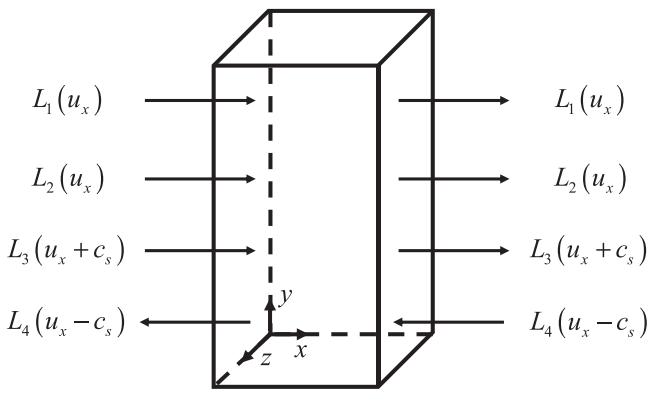

FIG. 1. Sketch of the direction of the characteristic velocities.

$$u_z^t = u_z^{t-1} - \delta t u_x^{t-1}\frac{\partial u_z^{t-1}}{\partial x}, \tag{64}$$

where the spatial derivatives in the wave amplitudes are modeled using a one-side second-order finite difference approach

$$\frac{\partial \mathbf{U}}{\partial x}(x_b) = \frac{1}{2\delta x}[3\mathbf{U}(x_b) - 4\mathbf{U}(x_{b-1}) + \mathbf{U}(x_{b-2})] + O(\delta x^2). \tag{65}$$

These derivations ultimately yield the macroscopic quantities of pressure and velocity at the outlet open boundary. Using the calculated pressure and velocity at the outlet open boundary, the equilibrium boundary scheme is applied to calculate the unknown particle distribution functions

$$f_{ijk} = \omega_{ijk}\frac{p}{c_s^2} + \omega_{ijk}\rho_0\left[\frac{\mathbf{e}_{ijk}\cdot\mathbf{u}}{c_s^2} + \frac{(\mathbf{e}_{ijk}\cdot\mathbf{u})^2}{2c_s^4} - \frac{|\mathbf{u}|^2}{2c_s^2}\right]. \tag{66}$$

2. Other boundaries

A no-slip boundary is implemented on both the pile surface and the bottom wall. On the curved pile surface, a second-order accuracy interpolation scheme proposed by Yu *et al.*[73] is used. In Fig. 2, the black solid line depicts the curved boundary, while the hollowed circles and the solid squares represent the fluid and the solid nodes, respectively. The distance in $\mathbf{e}_{ijk}$ direction between the first fluid node $\mathbf{x}_f$ and the solid boundary $\mathbf{x}_w$ is defined as q. The PDF for the wall in $\mathbf{e}_{ijk}$ direction is calculated by linear interpolation:

$$f_{ijk}(\mathbf{x}_w) = (1-q)f_{ijk}(\mathbf{x}_f) + qf_{ijk}(\mathbf{x}_s), \tag{67}$$

where the PDF at the solid node in $\mathbf{e}_{ijk}$ direction equals to the post-collision value at the fluid node $f_{ijk}(\mathbf{x}_s) = f^*_{\overline{ijk}}(\mathbf{x}_f)$. In the case of a

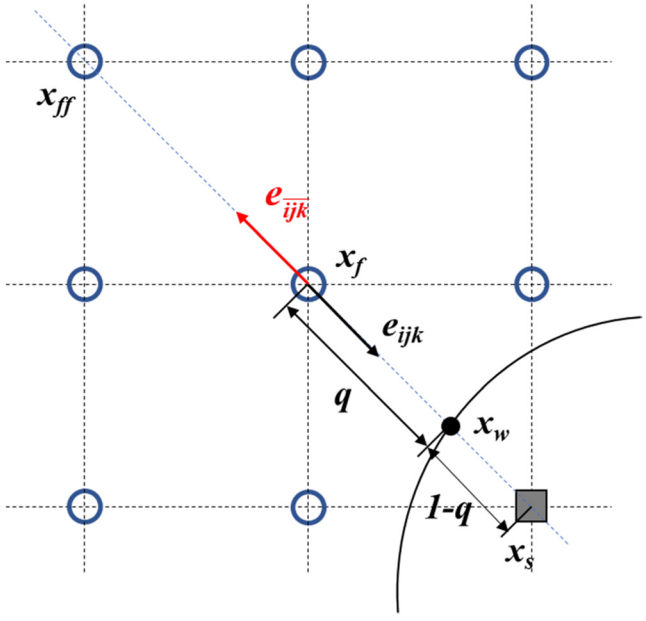

FIG. 2. Sketch of the implementation of the curved no-slip boundary condition.

stationary wall, the no-slip boundary condition is fulfilled by enforcing the PDF in the inverse direction $f_{\bar{i}\bar{j}\bar{k}}(\mathbf{x}_w) = f_{ijk}(\mathbf{x}_w)$. Then, the unknown PDF for the fluid node is calculated as follows:

$$f_{\bar{i}\bar{j}\bar{k}}(\mathbf{x}_f) = \frac{1}{1+q} f_{\bar{i}\bar{j}\bar{k}}(\mathbf{x}_w) + \frac{q}{1+q} f_{\bar{i}\bar{j}\bar{k}}(\mathbf{x}_{ff}). \tag{68}$$

The free-slip boundary condition is regarded as a simplification of the free surface in cases where the Froude number (Fr) is small. The free-slip boundary condition is implemented using the non-equilibrium extrapolation scheme[74]

$$f_{ijk}(\mathbf{x}_f, t+\delta_t) = f_{ijk}(\mathbf{x}_{ff}, t+\delta_t) + f^{eq}_{ijk}[p(\mathbf{x}_f, t), \mathbf{u}_{//}(\mathbf{x}_w, t)] - f^{eq}_{ijk}[p(\mathbf{x}_f, t), \mathbf{u}(\mathbf{x}_f, t)], \tag{69}$$

where $\mathbf{u}_{//}(\mathbf{x}_w, t)$ represents the tangential velocity, obtained from the first fluid node's velocity $\mathbf{u}(\mathbf{x}_f, t)$ and the normal direction of the boundary $\mathbf{n}$

$$\mathbf{u}_{//}(\mathbf{x}_w, t) = \mathbf{u}(\mathbf{x}_f, t) - [\mathbf{n} \cdot \mathbf{u}(\mathbf{x}_f, t)]\mathbf{n}. \tag{70}$$

III. COMPARISONS BETWEEN NUMERICAL RESULTS AND EXPERIMENTS

Simulations of flow past a circular cylinder at Re = 3900 are presented in this section. The numerical results are compared with the corresponding experimental data. The regularization form and regularization parameter in the CLBM model are also discussed in this section.

A. Flow past a circular cylinder at Re = 3900

The flow past a circular cylinder at Re = 3900 has been chosen to validate the cumulant lattice Boltzmann method (CLBM) model. This particular case has extensive experiment studies and abundant near wake experimental data[24,75] and serves as a benchmark case for numerical simulations utilizing various discretization methods such as the FDM,[24] FVM,[29,30] and HEM.[30] During these simulations, a range of turbulence models were employed, including the Smagorinsky model (SM),[24,29] k-equation model (KEM),[29] dynamic Smagorinsky model (DSM),[29] wall-adapting local eddy-viscosity model (WALE),[29,30] and implicit LES model (ILES).[30] Additionally, various grid types such as uniform grid[24] and curvilinear grid[29,30] were used. The Reynolds number is defined as $\mathrm{Re} = UD/\nu$ where the cylinder diameter $D = 0.1$ m and the uniform incoming velocity $U = 0.039$ m/s. Figure 3 depicts the sketch of our simulation domain. Table I shows the numerical setup of the present simulations. A uniform Cartesian grid with the same size in three directions $\Delta x = \Delta y = \Delta z$ is used. The grid resolutions are defined by the number of the grid N_D over the cylinder diameter D, which are $N_D = \{16, 32, 64\}$ referring to coarse, medium, and fine resolutions. For case 1-3, the preliminary validations employ a larger simulation domain: $20D$ along the streamwise direction (x axis), $20D$ along the transverse direction (y axis), and $4D$ along the spanwise direction (z axis). The distance from the cylinder's center to the inlet boundary is $L_0 = 5D$. For case 4, aiming to decrease simulation costs, a reduced simulation domain with $L_x \times L_y \times L_z = 15D \times 15D \times 3D$ and $L_0 = 4D$ is utilized. In all the cases, the origin is positioned at the cylinder's center. The simulation domains feature blockage ratios of 5% and 6.7%, aligning with the experimental blockage ratio range. Previous numerical studies have also indicated that the spanwise length significantly influences the recirculation region in simulations. Jiang and Cheng[30] recommended a spanwise length $L_z = 3D$ sufficient for $\mathrm{Re} > 2500$, a condition adequately met in this study. Given that velocity perturbations at the inlet were less than 0.7% in the experiment, a uniform velocity without turbulence is adopted for the inlet boundary. To minimize reflections, the CBC is implemented at the outlet boundary. Free-slip and periodic boundaries are applied in the transverse and spanwise directions, respectively. A curved no-slip boundary with second-order accuracy is set on the cylinder's surface.[73]

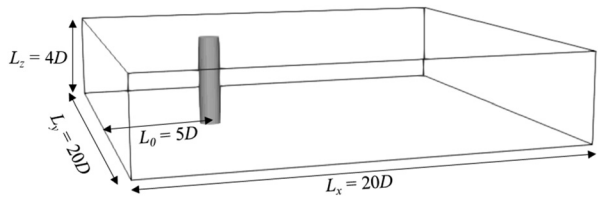

FIG. 3. Sketch of the simulation domain.

Each simulation was run for at least 800 non-dimensional time units $t^* = tU/D$. At the beginning, 200 time units were used for the flow development, and the remaining 600 time units (about 120 vortex shedding periods) were used to obtain the statistical results of the wake characteristics. The durations of the simulation and average time are long enough to account for the turbulence of the flow and are similar to former simulations.[30] The Mach number (Ma) is set as 0.064, satisfying the criterion of the incompressible limit $\mathrm{Ma} < 0.15$ in LBM simulations.[69] The regularization parameter is set to 0.1. Table II shows a comparison of the settings with other numerical methods. The main differences are that the CLBM simulations do not use any turbulence model in this case, and the first grid size near the cylinder pile is larger than the FVM method with second-order accuracy. In comparison with other high-order models, the CLBM model achieves fourth-order accuracy for the diffusion term using a completely local stencil, thereby preserving the inherent parallel scalability advantage of the LBM.

Several statistic quantities are defined to depict the flow characteristics and the forces on the cylinder pile like the Strouhal number St, drag coefficient C_D, lift coefficient C_L, and the pressure coefficient C_p:

$$\mathrm{St} = \frac{f_v D}{U}, \tag{71}$$

$$C_D = \frac{2F_D}{U^2 D L_z}, \tag{72}$$

$$C_L = \frac{2F_L}{U^2 D L_z}, \tag{73}$$

TABLE I. Numerical setup of the validation cases at Re = 3900.

Case	L_x/D	L_y/D	L_z/D	L_0/D	N_D
Case 1	20	20	4	5	16
Case 2	20	20	4	5	32
Case 3	20	20	4	5	64
Case 4	15	15	3	4	64

TABLE II. Simulation table and comparison of the simulation settings with other numerical methods.

Case	Method	High order	Grid type	First grid size	Turbulence model
P08 HR[24]	FDM	Yes	Uniform	$D/48$	SM
J21[30]	FVM	No	Curvilinear	$D/10\,000$	WALE
J21[30]	HEM	Yes	Curvilinear	$D/72$	ILES
T20[29]	FVM	No	Curvilinear	$D/880$	SM, KEM, DSM, WALE
Case 1	CLBM	Yes[a]	Uniform	$D/16$	No
Case 2	CLBM	Yes[a]	Uniform	$D/32$	No
Case 3	CLBM	Yes[a]	Uniform	$D/64$	No
Case 4	CLBM	Yes[a]	Uniform	$D/64$	No

[a]CLBM model employed here achieves fourth-order accuracy of the diffusion term.

$$C_p = \frac{2(p_b - p_\infty)}{U^2}, \tag{74}$$

where f_v represents the vortex shedding frequency, determined through the fast Fourier transformation (FFT) analysis of the C_L time series. F_D and F_L are the drag and lift forces exerted on the cylinder, respectively. The root mean square (rms) lift coefficient is defined as

$$C'_L = \sqrt{\frac{1}{N}\sum_{i=1}^{N}(C_{L,i} - \bar{C}_L)}, \tag{75}$$

where N is the number of measurement data. The non-dimensional recirculation region L_r/D and the minimum streamwise velocity $U_{\min}/U_c$ along the wake centerline of the cylinder are defined in Fig. 4. The formulation length of the maximum streamwise Reynolds normal stress $L_{u'u'}/D$ along the wake centerline of the cylinder is detailed in Fig. 5. The results of coarse, medium, and fine grid simulations (case 1-4) are compared with the experimental data and other simulations in Table III. While discrepancies were observed in the coarse grid simulation (case 1), the flow and force statistic parameters in the medium and fine grid simulations (case 2-4), such as St, C_D, C_p, are within the uncertainty range of the experiment measurements. Additionally, the absolute error, defined by $E_{sim} = |\phi_{sim} - \phi_{\exp,P08}|/\phi_{\exp,P08} \times 100\%$, is presented in Table IV. The absolute errors of the L_r/D, $U_{\min}/U_c$, $L_{u'u'}/D$ are 5.33%, 23.46%, and 4.74% for case 2, 3.2%, 11.73%, and 1.04% for case 3, and 0.47%, 8.8%, and 6.25% for case 4. Taking into account the uncertainty of the cutoff time average period (about 6% for 120 shedding period, as reported by Parnaudeau *et al.*[24]) in simulations, along with the uncertainty of the experiment measurements, the results of case 2-4 align well with the experimental data by Parnaudeau *et al.*[24] in the predicting of the length of the recirculation region L_r/D and location of the maximum Reynolds stress $L_{u'u'}/D$. The discrepancies of the $U_{\min}/U_c$ in our results can primarily be attributed to differences in the aspect ratio and blocking ratio between the simulations and experiments.

Figure 4 shows the time-averaged and spanwise-averaged streamwise velocity along the wake centerline. The velocity profiles of the medium (case 2) and fine grid simulations (case 3-4) agree well with the experimental data in the near wake region. No significant differences in the velocity profile were observed between the larger simulation domain (case 3) and the smaller one (case 4). The recirculation region is obviously larger than the experiment on the coarse grid (case 1) because the stair-step approximation of the cylinder surface is not sufficient on the coarse grid.

Figure 5 presents the streamwise Reynolds stress along the wake centerline. In the FDM simulation, only one peak is obtained, and

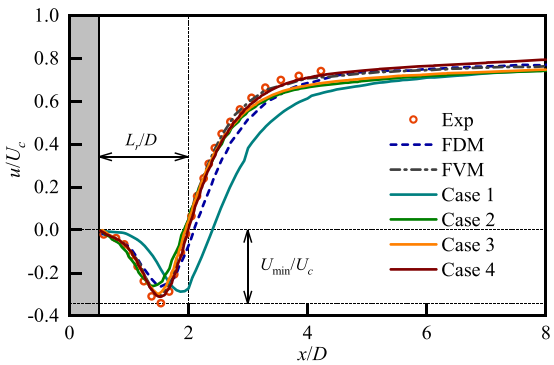

FIG. 4. Streamwise velocity along the wake centerline of the circular cylinder. Experimental data from the PIV result of Parnaudeau *et al.*[24]; FDM data from the HR LES result of Parnaudeau *et al.*[24]; FVM data from the L64-1 result of Ref. 29; HEM data from the reference case 6 result of Ref. 30; case 1-4 are the present CLBM simulations listed in Table I.

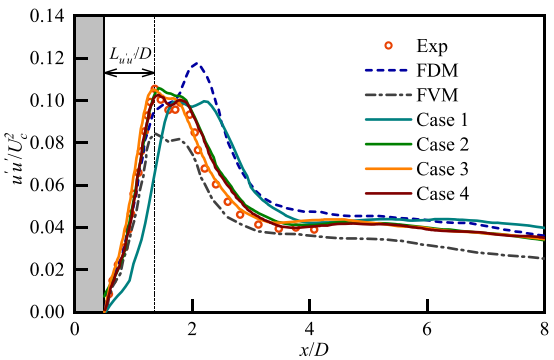

FIG. 5. Streamwise Reynolds normal stress along the wake centerline of the circular cylinder. Experimental and simulation data correspond to the same cases as those described in the caption for Fig. 4.

TABLE III. Comparison of the statistical flow parameters between the present numerical model, experimental data, and other numerical models.

Case	St	L_r/D	$U_{\min}/U_c$	$L_{u'u'}/D$	$\bar{C}_D$	C_p
Experiment						
P08[24]	0.208 ± 0.002	1.500	−0.341	0.864	···	···
L94[75]	0.215 ± 0.005	1.180	−0.24	···	0.98 ± 0.05	−0.90 ± 0.05
Simulation						
P08 HR[24]	0.208	1.584	−0.263	1.581	···	···
J21 OpenFOAM[30]	0.212	1.444	···	···	0.99	0.89
J21 Nektar++[30]	0.209	1.504	···	···	0.98	0.87
T20 L64-1[29]	···	1.450	−0.314	0.910	1.02	0.87
Case 1	0.197	1.897	−0.287	1.233	1.09	0.98
Case 2	0.206	1.420	−0.261	0.905	1.02	0.95
Case 3	0.207	1.452	−0.301	0.855	1.01	0.93
Case 4	0.210	1.493	−0.311	0.918	0.96	0.89

there is a slight step in front of it. Also, the location of the maximum Reynolds stress $L_{u'u'}/D$ in the FDM results is about 83% larger than that observed in the experiment. In the FVM simulation, the peak pattern shows consistency with the experimental data, while the amplitude is significantly underestimated. The Reynolds normal stress values from the FVM results align with the large field of view particle image velocimetry (PIV) data from experiments. However, the authors of the experiments noted that the measurement accuracy of larger field of view is less than that the smaller one, primarily because a smaller PIV estimation window yields more precise turbulence statistics.[24] Therefore, the PIV data from the smaller field of view are selected for presentation in Fig. 5. Our medium (case 2) and fine grid simulations (case 3-4) using CLBM perfectly capture the two-peak shape and the peak values of the Reynolds normal stress in the near wake, significantly outperforming the simulations using FDM and FVM. Similar to Fig. 4, the coarse grid result (case 1) has a larger formation length. The reason has already been mentioned in the above paragraph, and the coarse grid results will be omitted in the following figures.

The time-averaged and space-averaged velocity components at various wake locations $x/D = 1.06$, 1.54, 2.02 in the numerical simulations are compared with the experimental data in Fig. 6. A notable transformation in the shape of the streamwise velocity profile occurs within the recirculation region. In the near wake region $x/D = 1.06$ [Fig. 6(a)], the streamwise velocity profile exhibits a U-shape, which transforms into a V-shape at further downstream locations at $x/D = 1.54$, 2.02 [Figs. 6(b) and 6(c)]. The transverse velocity profiles at various locations [Figs. 6(d)–6(f)] display anti-symmetry relative to the $y/D = 0$ plane. Our fine grid results (case 3-4) show excellent agreement with the experimental data at each profile in the wake of cylinder for both the streamwise and transverse velocity when compared with other numerical simulations. There is no clear difference between larger simulation domain results (case 3) and smaller simulation domain results (case 4). The medium grid result (case 2) also accurately predicts most features in the wake, albeit with minor discrepancies in the streamwise velocity at $x/D = 2.02$ [Fig. 6(c)] and the transverse velocity at $x/D = 1.54$ [Fig. 6(e)]. The overall discrepancy of the medium grid results (case 2) is comparable to that of the FDM result, which are deemed acceptable.

TABLE IV. The absolute error of the different numerical simulations.

Case	$E_{L_r/D}$(%)	$E_{U_{\min}/U_c}$(%)	$E_{L_{u'u'}/D}$(%)
P08 HR[24]	5.60	22.87	82.99
J21 OpenFOAM[30]	3.73	···	···
J21 Nektar++[30]	0.27	···	···
T20 L64-1[29]	3.33	7.92	5.32
Case 2	5.33	23.46	4.74
Case 3	3.20	11.73	1.04
Case 4	0.47	8.80	6.25

Figure 7 displays the lateral distribution of the Reynolds stress components at various near wake locations. In the case of the streamwise Reynolds normal stress [Fig. 7(a)–7(c)], two distinct peaks are evident, resulting from flow separation and shear layers. Downstream of the recirculation region, these two peaks overlap due to vortex formation. For the transverse Reynolds normal stress [Figs. 7(d)–7(f)], the maximum value is located on the centerline. For the Reynolds shear stress [Figs. 7(g)–7(i)], its profile is also anti-symmetric and mirrors the pattern observed in the transverse velocity. To sum up, except for a slight underestimation in the peak of the streamwise Reynolds normal stress at $x/D = 1.06$, the fine grid simulations (case 3-4) align well with the experimental data for all the Reynolds stress components. The results from the larger simulations domain (case 3) show a slight advantage over those from the smaller domain (case 4) regarding the transverse Reynolds normal stress at $x/D = 1.54$, 2.02. The medium grid result (case 2) underestimated some Reynolds stress components but still demonstrated similar accuracy compared to the FDM, FVM, and HEM simulations.

Figure 8 shows the power spectra of the transverse velocity fluctuations at $x/D = 3$. The Welch periodogram technique is used to estimate the power spectra. The velocities are collected over 120 vortex shedding cycles with about 80 000 samples. The vortex shedding frequency f_v is used to normalize the frequency analyzed by FFT. The first peak at the fundamental frequency $f/f_v = 1$ and the second peak at the second harmonic frequency $f/f_v = 3$ are obvious in the power spectra of the transverse velocity fluctuations. Three subranges of the

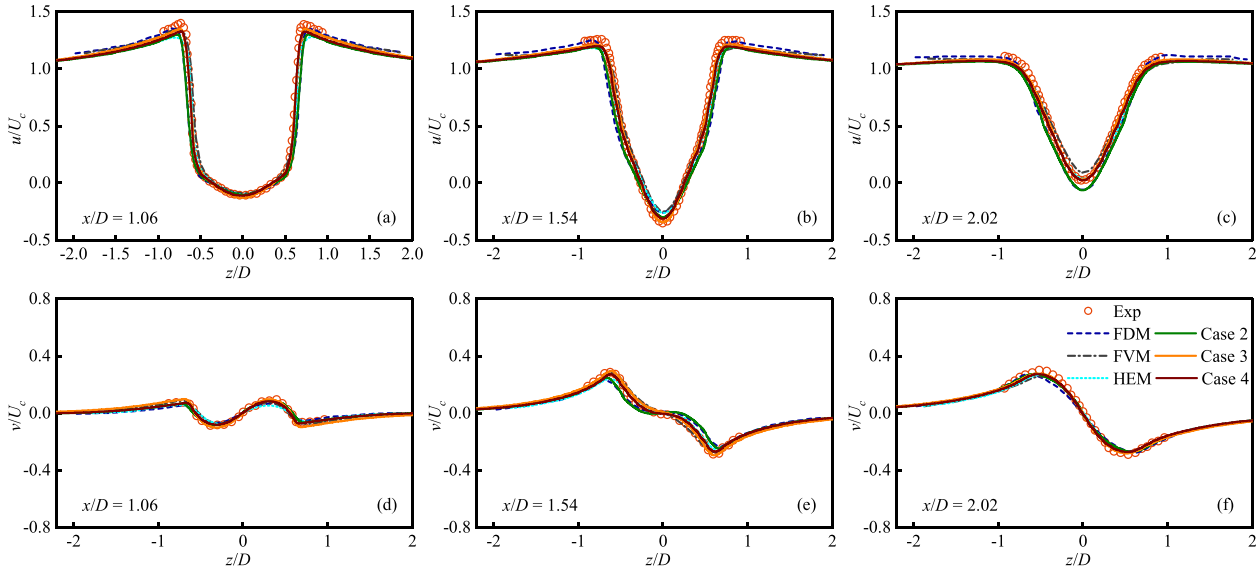

FIG. 6. Lateral profiles of the velocity in the wake region of the circular cylinder at $x/D = 1.06$, 1.54, 2.02. (a)–(c) Streamwise velocity and (d)–(f) transverse velocity. Experimental and simulation data correspond to the same cases as those described in the caption for Fig. 4.

power transformation are clearly shown in both the medium (case 2) and fine grid simulations (case 3). No significant differences appear in the narrow inertial range, with both simulations following Kolmogorov's law in this range. However, the medium grid simulation (case 2) dissipates energy faster than the fine grid simulation (case 3) in the dissipation range, which is consistent with the former results.

Up to this point, the CLBM model with a constant regularization parameter has undergone thorough validation for subcritical flow over a circular cylinder. The fine grid simulation (case 3-4) perfectly predicts the near wake statistic information without using any turbulence model, while the medium grid simulation (case 2) also gets acceptable results when compared with other numerical models.

B. Analysis of the regularization parameter

In the present parameterized CLBM model, the regularization parameter is the only free parameter. The original purpose of the regularization process, imposed on the third-order cumulants, is to improve the stability of the model in small viscosity and high Reynolds number cases, which are common in practical engineering flows with the media of water ($\nu = 1 \times 10^{-6}$ m^2/s).[51] Furthermore, through benchmark cases analysis, the regularization process also acts as an implicit sub-grid scale model, dissipating higher frequency energy in the power spectra.[65,68,76] With these features, the CLBM model is proven capable of simulating high Reynolds number cases with relatively coarser resolution (about $y^+ < 50$) even without using any explicit turbulence models.[61] In the test cases mentioned above in Sec. III, the regularized relaxation rates are calculated in accordance with the original formulation by Geier *et al.*[51] However, the regularization parameter is fixed at a larger constant value of 0.1 for larger Reynolds number and coarser resolution cases, as opposed to the default value of 0.01 proposed by Geier *et al.*[51] In the heuristic work by Gehrke and Rung,[67] they propose a resolution-related regularization parameter, derived through dimensional analysis from a series of turbulent channel flow benchmark cases

$$\lambda_m = \frac{\mathrm{Re}_{\Delta x}}{10\mathrm{Ma}}, \tag{76}$$

where $\mathrm{Re}_{\Delta x} = U_c \Delta x/\nu$ is defined as the grid Reynolds number which reflects the grid resolution. The resolution-depended regularized relaxation rates are calculated as follows:

$$\omega^m_{3,1} = \omega_3(1 + \lambda_m|C_{120} + C_{102}|), \tag{77}$$
$$\omega^m_{3,2} = \omega_3(1 + \lambda_m|C_{210} + C_{012}|), \tag{78}$$
$$\omega^m_{3,3} = \omega_3(1 + \lambda_m|C_{201} + C_{021}|), \tag{79}$$
$$\omega^m_{4,1} = \omega_4(1 + \lambda_m|C_{120} - C_{102}|), \tag{80}$$
$$\omega^m_{4,2} = \omega_4(1 + \lambda_m|C_{210} - C_{012}|), \tag{81}$$
$$\omega^m_{4,3} = \omega_4(1 + \lambda_m|C_{201} - C_{021}|), \tag{82}$$
$$\omega^m_{5} = \omega_5(1 + \lambda_m|C_{111}|). \tag{83}$$

Note that this regularization parameter vanishes at low Reynolds number and in the fully-resolved limit. This modification aims to eliminate the sole free parameter in the CLBM model.

The original regularization process with various regularization parameters and the parameter-free regularization process are tested using the case described in Sec. III A. The simulation cases are listed in Table V.

The streamwise velocity in the wake centerline with different regularization parameters is shown in Fig. 9. When using the original form of the regularization proposed by Geier *et al.*,[51] the results of the different regularization parameters converge for improved resolution [Fig. 9(b)], and the divergence of the medium resolution is not significant [Fig. 9(a)]. Focusing on the new form of the regularization proposed by Gehrke and Rung[67] with the default regularization parameter in Eq. (76), the results align with the default regularization form at

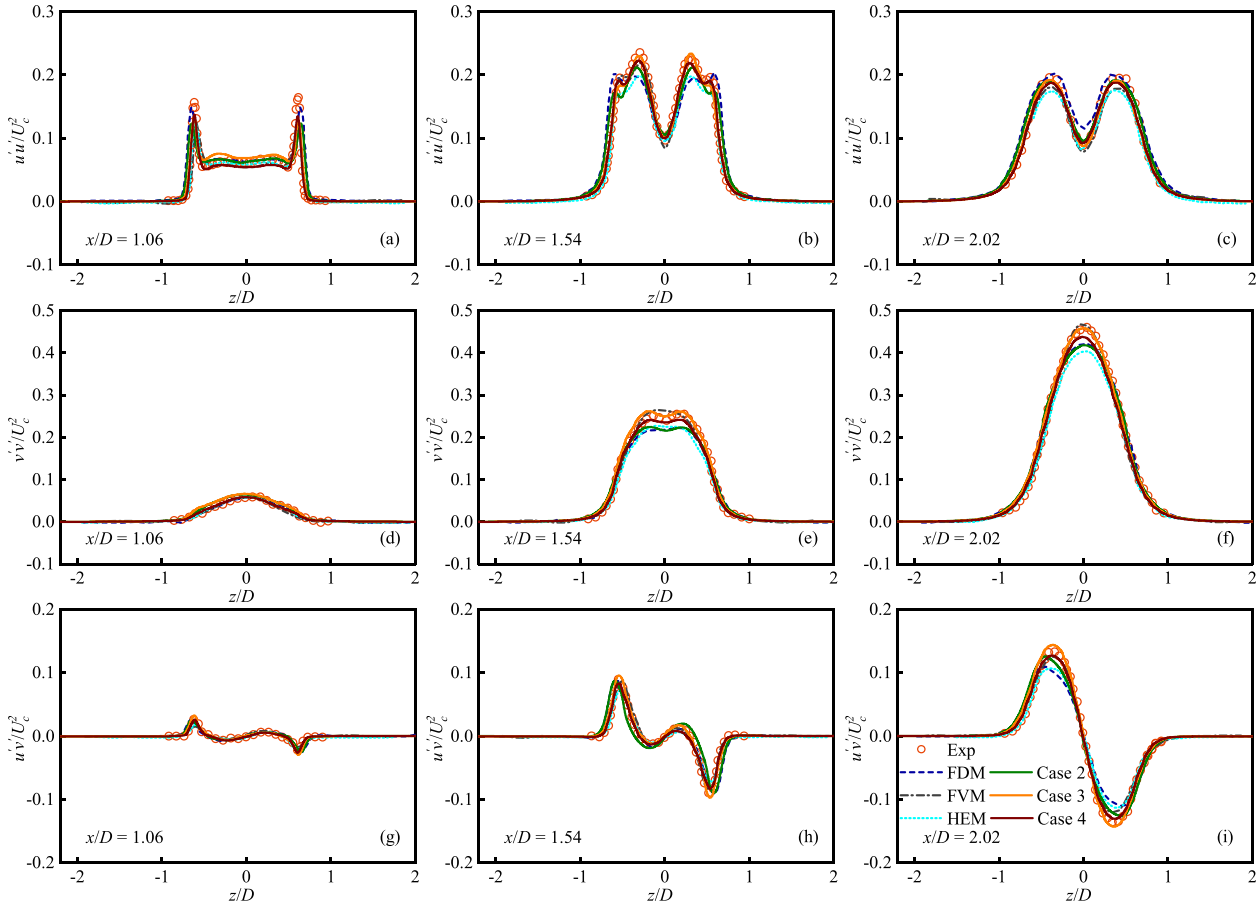

FIG. 7. Lateral profiles of the Reynolds stress in the wake region of the circular cylinder at $x/D = 1.06$, 1.54, 2.02. (a)–(c) Streamwise Reynolds normal stress, (d)–(f) transverse Reynolds normal stress, and (g)–(i) Reynolds shear stress. Experimental and simulation data correspond to the same cases as those described in the caption for Fig. 4.

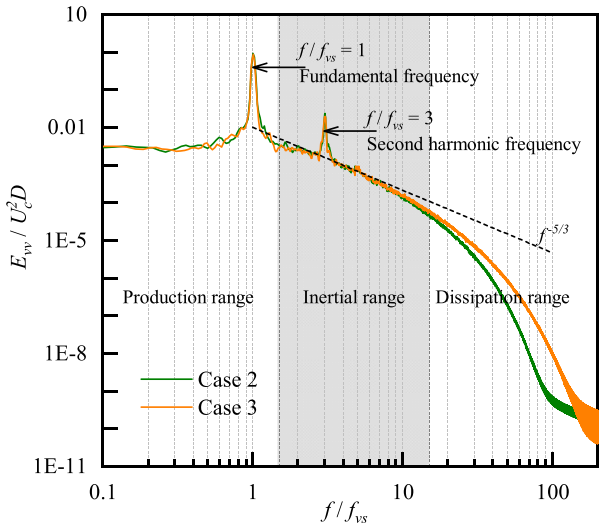

FIG. 8. Power spectra of the transverse velocity fluctuations at $x/D = 3.0$.

high resolutions. However, noticeable deviations from experimental data occur at medium resolution. The objective to auto-adjust the free parameter with grid resolution remains unmet. The primary reason is attributed to the default regularization parameter in Eq. (76), derived from a series of flow-attached turbulence channel flow simulations. Although the heuristic work by Gehrke and Rung[67] introduces a resolution-sensitive regularization form with the regularization parameter $\lambda_m \sim \mathrm{Re}_{\Delta x}/\mathrm{Ma}$, the relationship between the regularization parameter λ_m and the resolution-sensitive term $\mathrm{Re}_{\Delta x}/\mathrm{Ma}$ is still case-dependent, as evidenced by our investigation. This implies that the regularization form by Gehrke and Rung[67] is not entirely parameter-free and leaves a case-dependent factor χ for the regularization parameter λ_m

$$\lambda_m = \chi \frac{\mathrm{Re}_{\Delta x}}{\mathrm{Ma}}. \tag{84}$$

In Fig. 10, the detailed relationship between the absolute value of the third-order cumulant $|C_{210} + C_{012}|$ and the relevant relaxation rate $\omega_{3,2}$ is shown as an example at medium resolution $N_D = 32$ and other third-order cumulants and relaxation rates show the same tendency.

TABLE V. Simulation cases for regularization parameter analysis.

Case	N_D	λ	λ_m	$\mathrm{Re}_{\Delta x}$	Ma
Case 2-1	32	0.01	···	121.88	0.064
Case 2-2	32	0.05	···	121.88	0.064
Case 2-3[a]	32	0.1	···	121.88	0.064
Case 2m	32	···	190.43	121.88	0.064
Case 3-1	64	0.01	···	60.94	0.064
Case 3-2	64	0.05	···	60.94	0.064
Case 3-3[a]	64	0.1	···	60.94	0.064
Case 3m	64	···	95.21	60.94	0.064

[a]Case 2-3 and case 3-3 refer to case 2 and case 3 in Table II, respectively.

The third-order cumulant $|C_{210}+C_{012}|$ is on the order of $O(10^{-4})$ in the present case; therefore, when the regularization parameter in Eq. (40) is on the order of $O(10^{-2}) \sim O(10^{-1})$, the third-order cumulant $|C_{210}+C_{012}|$ in the denominator is negligible, and the relaxation rate $\omega_{3,2}$ increases monotonically with the increase in $|C_{210}+C_{012}|$ in Eq. (40). Then, the post-collision third-order cumulant $|C^*_{210}+C^*_{012}|$ decreases when the relaxation rate $\omega_{3,2}$ increases, as shown in Eq. (15), indicating that less of the non-equilibrium part is retained in the collision process. This same tendency appears in the regularization form proposed by Gehrke and Rung[67] in Eq. (78). Furthermore, when comparing different regularization parameters, the relaxation rate $\omega_{3,2}$ decreases as the regularization parameters λ increases. Therefore, more of the non-equilibrium part is retained in the collision process as λ increases. Combining this with the information in Fig. 9, it is reasonable to infer that a larger absolute value of the post-collision third-order cumulant leads to a smaller recirculation region and reduced reverse velocity.

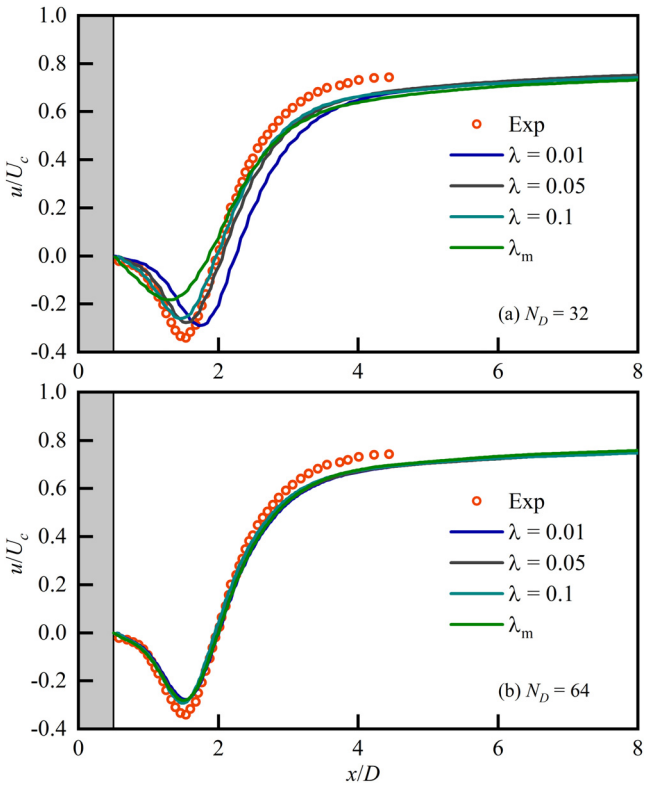

FIG. 9. Influence of the regularization parameter on different grid resolutions. Streamwise velocity along the wake centerline of the case described in Sec. III A. (a)$N_D = 32$; (b)$N_D = 64$.

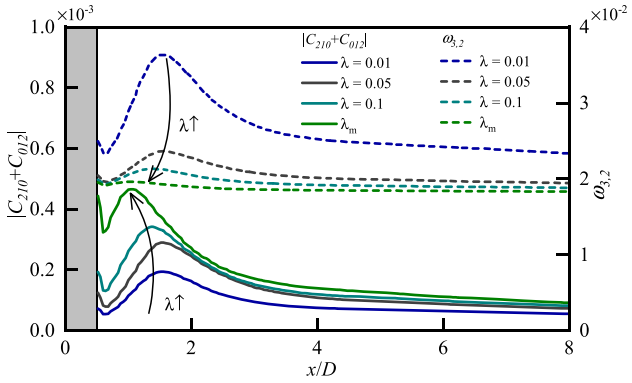

FIG. 10. The third-order cumulant $|C_{210}+C_{012}|$ and relevant relaxation rate $\omega_{3,2}$ along the wake centerline for $N_D = 32$ case with different regularization parameters.

IV. NUMERICAL INVESTIGATIONS FOR Re = 3900 TO 2×10^5

After the verification of the CLBM model at Re = 3900, further analyses of flow past a circular cylinder within the subcritical range of Re = 3900 to 2×10^5 were conducted. Experiment setups and measured physical quantities in this range are detailed in Table VI. These experiments provide extensive data. Numerical simulations employing different numerical methods (like FDM, FVM, and HEM) and different turbulence models (like URANS/RANS, DES, LES, and ILES) in this range are summarized in Table VII. These simulations were conducted on commercial softwares[32,36] (such as Fluent and Star-CCM+), open-source codes[29–35] (such as OpenFOAM and Nektar++), and in-house codes[24,27,28,42] (such as CFDShip-Iowa).

Table VIII outlines the simulation setup using the CLBM model. Six cases of Re = 8000, 10 000, 20 000, 40 000, 100 000, and 200 000 are used to examine flow properties and hydrodynamic forces variations within the subcritical range. Uniform grids of $N_D = 64$ are used for case 4-8 and $N_D = 96$ are used for case 9-10. To minimize the total grid number, a smaller simulation domain that is validated in Sec. III A is employed. The total grid numbers are approximately 1.84×10^8 and 6.27×10^8 for $N_D = 64$, 96, respectively. The y^+ value adjacent to the cylinder's surface is estimated following the method in Stahl *et al.*[78]. For case 4-10, the maximum y^+ value on the cylinder's surface ranges from 5 to 86. Only in case 10, the maximum y^+ value exceeds the criteria of $y^+ < 50$ outlined in the previous CLBM study.[61]

A. Instantaneous flow field

The instantaneous three-dimensional vortex structures along with the dimensionless wall distance y^+ value on the circular cylinder's surface across various Re are shown in Fig. 11. The vortices are

TABLE VI. Summary of experimental studies within the range of Re = 3900 to 2×10^5.

References	Re($\times 10^4$)	Aspect ratio	Blockage(%)	Tu(%)	Measured quantities
Gerrard[13,14]	0.4–18	7–80	1–15	0.3	C_D, C'_L, St
Keefe[77]	0.03–10	3/18	0.8	...	C_D, C'_L, St
Son and Hanratty[15]	0.5–10	...	...	...	St
Moeller[16]	0.5–5.6	16/19	...	0.3	C'_L
Schewe[17]	2–710	10	10	0.4	C_D, St
Norberg and Sunden[18]	1.8–30	12/8.8	4/11	0.06	C'_L, C_{pb}, St
Szepessy and Bearman[11]	0.9–14	0.25–12	7.7	0.05	C_D, C'_L, C_p
West and Apelt[19]	1.1–22	15–35	4–10	0.2	C_D, C'_L
Norberg[20]	0.005–4	5–50	1.6	0.1	C_{pb}, St
Norberg[21]	0.15–1	65	1.5	0.1	L_r
MARIN[22]	3–80	18.6	...	...	C_D
Dong *et al.*[23]	0.39–1.0	8.78	8.3	0.1	C_D, C'_L, C_{pb}, St
Parnaudeau *et al.*[24]	0.39	20	4.3	...	St, L_r
Molochnikov *et al.*[25]	0.39	10	13	0.25	L_r

TABLE VII. Summary of numerical simulations within the range of Re = 3900 to 2×10^5.

References	Re($\times 10^4$)	Method	2D/3D	Turbulence model	First grid size
Kravchenko and Moin[42]	0.39	B-spline	3D	LES	$D/172$
Parnaudeau *et al.*[24]	0.39	FDM	3D	LES	$D/48$
Lysenko *et al.*[31]	2	FVM	3D	LES	$D/1786$
Stringer *et al.*[32]	0.004–100	FVM	2D	URANS	Not mentioned
Prsic *et al.*[33]	0.39, 1.31	FVM	3D	LES	$y^+ < 2$
Lloyd and James[34]	6.31–50.6	FVM	3D	LES	$y^+ = 0.5$
Yeon *et al.*[27]	6.31–75.7	FDM	3D	LES	$y^+ = 0.03$–0.67
Ye and Wan[35]	6.31–75.7	FVM	2D	RANS	$y^+ = 1$–5
Wen and Qiu[36]	6.31–75.7	FVM	2D/3D	RANS/DES/LES	$y^+ = 0.15$
Cheng *et al.*[28]	0.39–85	FDM	3D	LES	$y^+ = 0.83$–1.93
Qiu *et al.*[37]	6.31–75.7	FVM	2D	RANS	Not mentioned
Tian and Xiao[29]	0.39	FVM	3D	LES	$D/880$
Jiang and Cheng[30]	0.39	FVM	3D	LES	$D/10\,000$
	0.04–0.39	HEM	3D	ILES	$D/72$

TABLE VIII. Numerical setup of the simulations using the CLBM for Re = 3900 to 2×10^5.

Case	Re ($\times 10^4$)	Total time unit	Statistical time unit	Vortex shedding period	N_D
Case 4	0.39	600	400	120	64
Case 5	0.8	600	400	120	64
Case 6	1.0	600	400	120	64
Case 7	2.0	600	400	120	64
Case 8	4.0	600	400	120	64
Case 9	10.0	600	400	120	96
Case 10	20.0	600	400	120	96

visualized by means of the Q-criterion. In the subcritical range of Re = 3900–2×10^5, vortex shedding apparently exhibits a three-dimensional nature. The parallel shear layers roll-up in the downstream and eventually form alternating vortices shedding in the near wake. As Re increases, the turbulent transition point in the shear layers shifts upstream. This shift results in a reduced formation length for the mean recirculation region L_r. At Re = 3900, elongated streamwise vortex structures appear in the near wake, transitioning to smaller, more chaotic structures with an increase in Re. Throughout this range of Re, the streamwise distances between the shedding vortices remain nearly constant.

Figure 12 depicts the instantaneous velocity field at different Re, highlighting the highly turbulent and divergent wake flow behind the circular cylinder. At Re = 3900, the transition from laminar to

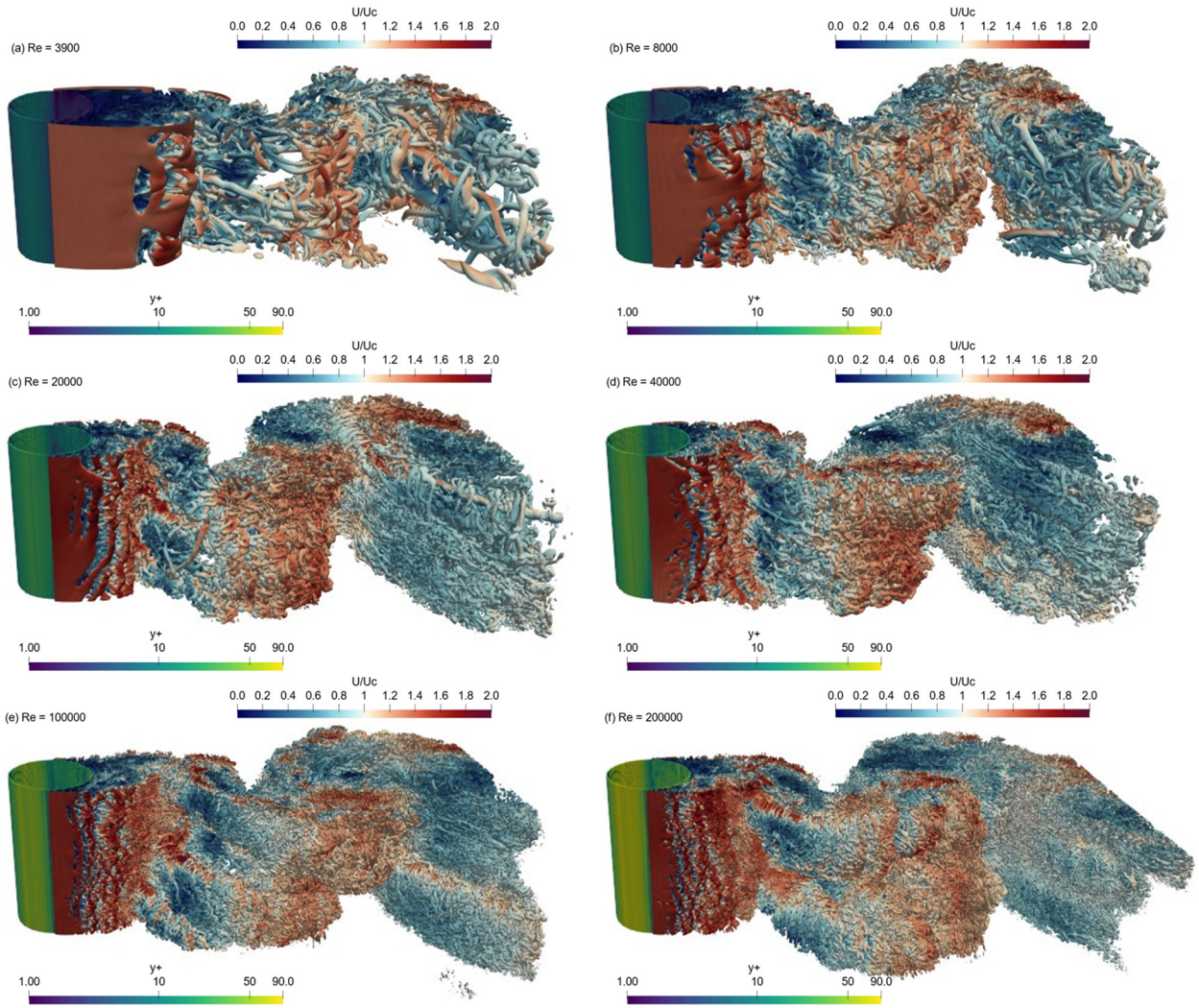

FIG. 11. Instantaneous vortex structure in the near wake and the dimensionless wall distance y^+ value on the circular cylinder surface. Vortices represented by the contour of Q-criterion with $Q = 10$ and colored by the scaled velocity. (a) Re = 3900; (b) Re = 8000; (c) Re = 20 000; (d) Re = 40 000; (e) Re = 100 000; and (f) Re = 200 000.

turbulent shear layers occurs further downstream, resulting in a larger recirculation region. With the developing of the shear layer instability as the increase in Re, the Kelvin–Helmholtz vortices are noticeable in the shear layer and the separated flow rapidly sheds from both sides of the cylinder. Within the subcritical range of Re = 3900–2×10^5, variations in the separation angle are not markedly apparent.

Figure 13 displays the instantaneous pressure field in the near wake. With the Re increased in from 3900 to 2×10^5, the low-pressure regions become closer to the cylinder. Additionally, the pronounced curvature of pressure contours near the cylinder suggests increased pressure fluctuations in this vicinity.

B. Mean flow field

Figure 14 shows the time-averaged and spanwise-averaged streamwise velocity profile along the wake's centerline for varying Re from 3900 to 2×10^5. In this range, both the non-dimensional recirculation region L_r/D and the minimum streamwise velocity $U_{\min}/U_c$ along the wake centerline of the cylinder exhibit a monotonic decrease as Re increases. This trend is linked to the earlier transition to turbulence in the shear layers, as illustrated by the instantaneous flow fields depicted in Figs. 11 and 12.

The L_r − Re relationship obtained from our CLBM simulations is shown in Fig. 15 in the range of Re = 3900 to 2×10^5. Due to the challenges in measuring circulation, quantitative experimental data within this range are limited. To quantitatively analyzed the relationship between the shear layer instability and the length of the recirculation region, the instability of the shear layer is characterized by the maximum Reynolds shear stress $(u'v'/U_c^2)_{\max}$ in the near wake. Figure 16 depicts the $(u'v'/U_c^2)_{\max}$ − Re relationship. The maximum Reynolds shear stress increases prominently in the range of Re = 3900–10 000 and increases slowly in the range of Re = 10 000–200 000. An evident

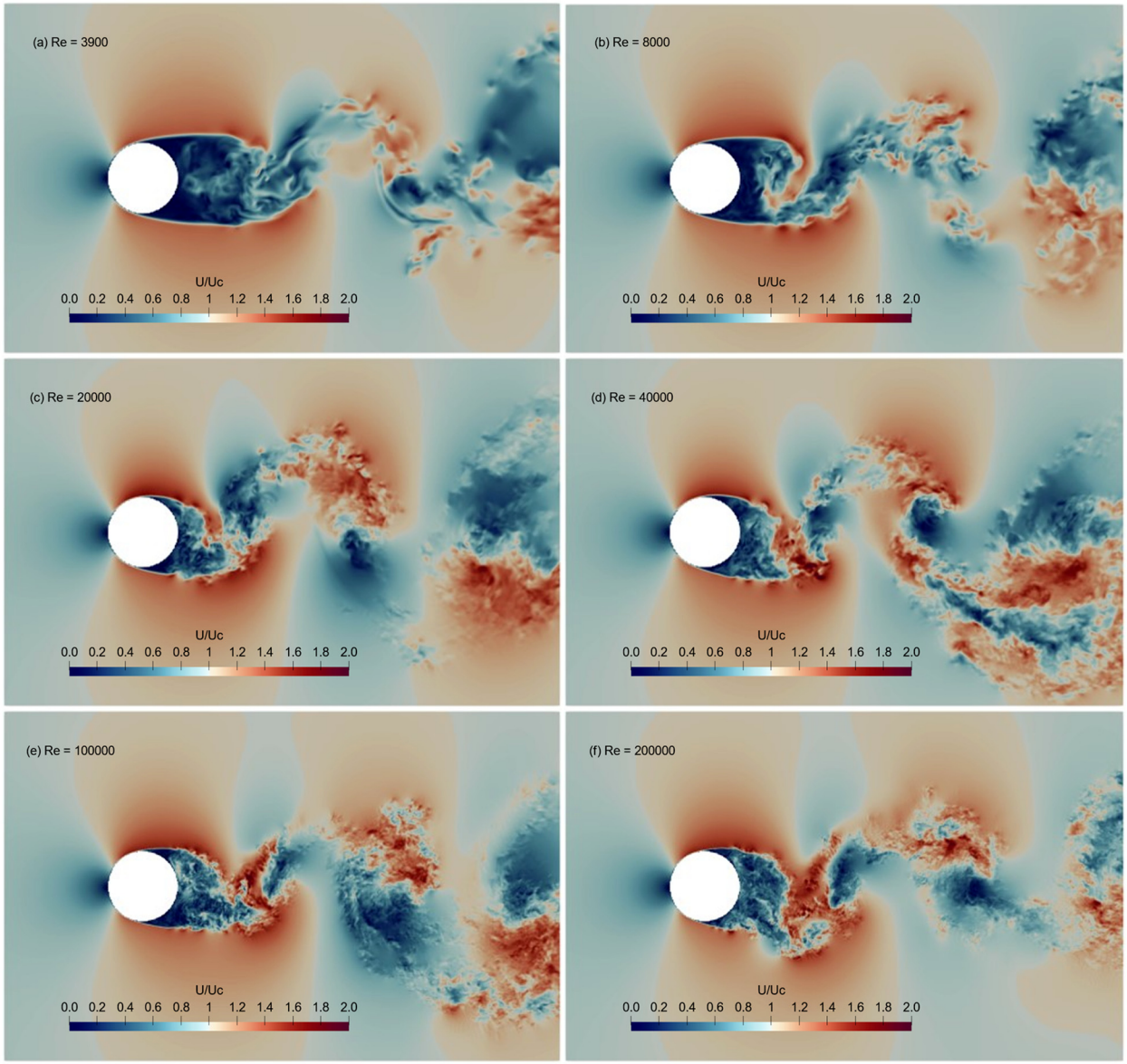

FIG. 12. Instantaneous velocity field in the near wake. The velocity is scaled by the inlet velocity. (a) Re = 3900; (b) Re = 8000; (c) Re = 20 000; (d) Re = 40 000; (e) Re = 100 000; and (f) Re = 200 000.

inverse correlation between the relationships of $(u'v'/U_c^2)_{\max} - \mathrm{Re}$ and $L_r - \mathrm{Re}$ in the range of $\mathrm{Re} = 3900$ to 2×10^5, which effectively quantifies the observed qualitative phenomenon in the instantaneous flow field.

C. Hydrodynamic forces

The variation in the drag coefficient $\bar{C}_D$ on Re is not obvious in the range of $\mathrm{Re} = 3900$ to 2×10^5 as shown in Fig. 17. It should be noticed that the precise threshold of the subcritical and critical ranges remains elusive. The beginning of the "drag crisis" phenomenon is observed around $\mathrm{Re} = 2 \times 10^5$ in some of the experiments. In the present CLBM simulation at $\mathrm{Re} = 2 \times 10^5$, flow separation remains symmetrical, with no evident separation bubbles occurred on the cylinder's sides. This observation might be due to insufficient resolution, as indicated by the maximum y^+ value exceeding the criteria of $y^+ < 50$ at $\mathrm{Re} = 2 \times 10^5$. Due to the limit of the computing cost associated with uniform grids, the finer resolution simulations of this case will be addressed to the future work. The current CLBM results are in strong concordance with experimental data for $\mathrm{Re} = 3900$ to 1×10^5, contrasting with some numerical models that either underestimate the drag coefficient or prematurely indicate a drag crisis within this Re range. This underscores the capability of the CLBM model in

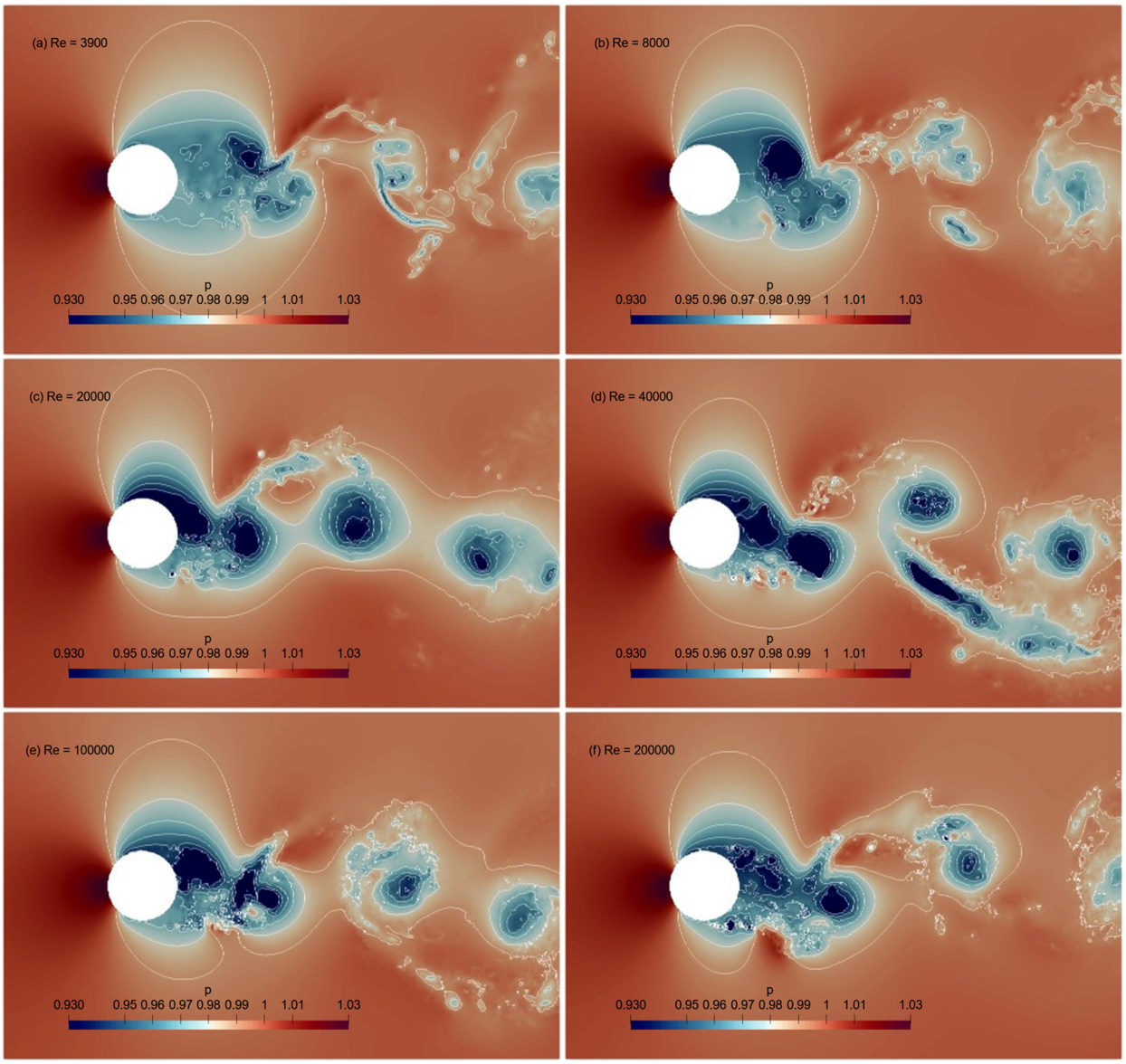

FIG. 13. Instantaneous pressure field and pressure contours in the near wake. The pressure is scaled by the inlet pressure. (a) Re = 3900; (b) Re = 8000; (c) Re = 20 000; (d) Re = 40 000; (e) Re = 100 000; and (f) Re = 200 000.

simulating flow past a circular cylinder at relatively coarser grid resolution (up to $y^+ \approx 50$), compared with other numerical method.

For the $C'_L - \mathrm{Re}$ relationship, observed scatter across experiments is attributed to the differences in aspect ratio[11] (L/D) and force measurement techniques.[27] Szepessy and Bearman[11] highlight the aspect ratio's significant impact on fluctuating lift force. In most of the simulations, the aspect ratio is set to 3 or π for $\mathrm{Re} > 2500$. This setting is sufficient for other variations, but the C'_L decreases with increasing aspect ratio. To validate the simulation results, experimental data with comparable aspect ratio $L/D = 3$ from Keefe[77] and $L/D = 2.5$ from Szepessy and Bearman[11] are added in Fig. 18. The simulation results of the present CLBM model agree well with these experimental data and show correct trend in the range of $\mathrm{Re} = 3900$ to 2×10^5 compared to other numerical models. Furthermore, the $C'_L - \mathrm{Re}$ shows inverse correlation with the $L_r - \mathrm{Re}$. This is attributed to the upstream movement of the low-pressure region as the Re increases, causing increased lift force fluctuation due to vortex shedding, as evidenced in the instantaneous pressure field in Fig. 13.

The base pressure coefficient $-C_{pb}$ variation with Re from 3900 to 2×10^5 aligns with the experimental data, as Fig. 19 illustrates. The variation in the pressure coefficient along the cylinder surface is depicted in Fig. 20. The base pressure coefficient is primarily affected

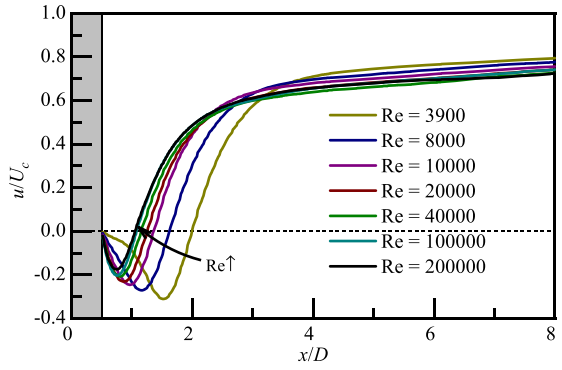

FIG. 14. Streamwise velocity along the wake centerline of the circular cylinder at different Reynolds number.

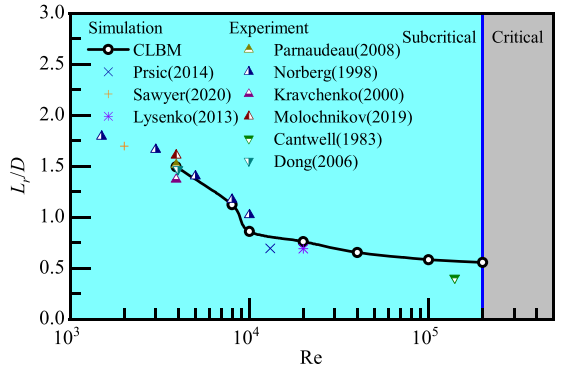

FIG. 15. The relationship between the dimensionless length of the recirculation region L_r/D and Re in the range of Re = 3900 to 2×10^5.

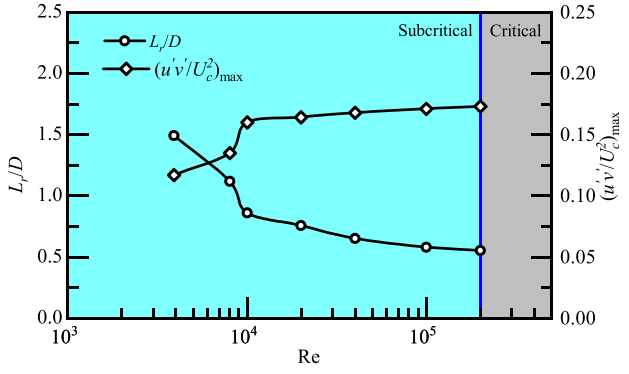

FIG. 16. The relationship between the maximum Reynolds shear stress $(u'v'/U_c^2)_{max}$ and Re in the range of Re = 3900 to 2×10^5. The result is compared with the L_r − Re relationship.

by the low-pressure region due to vortex formation. A direct relationship exists between the proximity of the cylinder's base point to the low-pressure area and the magnitude of the base pressure coefficient. The low-pressure location correlates positively with L_r − Re in Fig. 21,

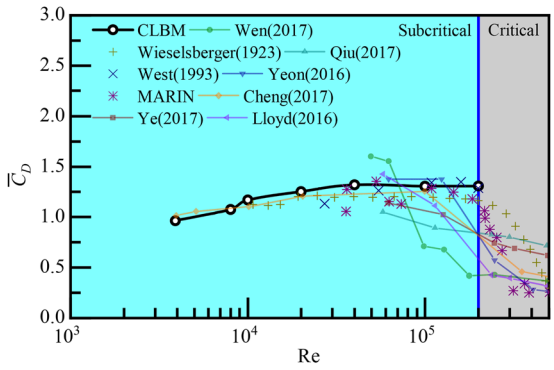

FIG. 17. The relationship between the drag coefficient $\bar{C}_D$ and Re in the range of Re = 3900 to 2×10^5. The scatters represent experimental data. The lines with the solid symbol represent simulation results of other models. The line with hollow symbol represents the present CLBM results.

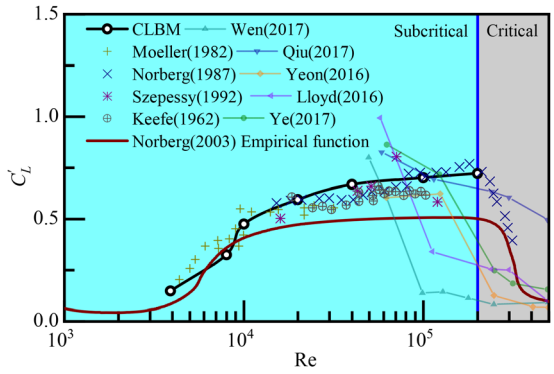

FIG. 18. The relationship between the root-mean-squared lift coefficient C'_L and Re in the range of Re = 3900 to 2×10^5. The scatters represent experimental data. The solid line represents an empirical function. The lines with solid symbol represent simulation results of other models. The line with hollow symbol represents the present CLBM results.

implying an inverse correlation between $-C_{pb}$ − Re and L_r − Re in the examined range.

Figure 22 illustrates minimal variation in St across the Re range investigated. This consistency is accurately captured by the current CLBM simulations, in contrast to some other numerical models that do not replicate this feature successfully.

V. DISCUSSION ON THE COMPUTATIONAL EFFICIENCY AND PARALLEL SCALABILITY

The numerical models based on the LBM are known as their superior parallel scalability and computational efficiency compared to those based on other numerical methods.[45,46] The current CLBM model, benefiting from high-order accuracy for the diffusion term achieved through an entirely local stencil, inherits all LBM advantages. The parallel scalability and computational efficiency of the present model are compared with other general models (such as OpenFOAM and Nektar++) in this section, using the reference case of Re = 3900 in Sec. III A.

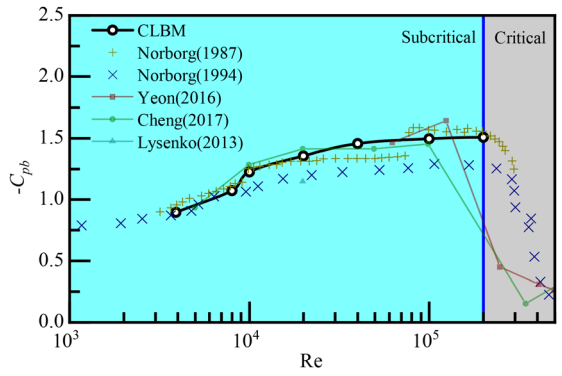

FIG. 19. The relationship between the base pressure coefficient $-C_{pb}$ and Re in the range of Re = 3900 to 2×10^5. The scatters represent experimental data. The lines with solid symbol represent simulation results of other models. The line with hollow symbol represents the present CLBM results.

The numerical settings align with case 4 in Sec. III A. All the simulations were conducted using our in-house code[45] with integrated Message Passing Interface (MPI)/OpenMP technique and run on a supercomputer with two Intel(R) Xeon(R) Gold 6348 CPUs (28 cores per processor) per computing node. The comparisons of the speedup ratio and computational efficiency are shown in Table IX. In Table IX, case 4-1 to case 4-6 represent the parallel computations using different numbers of computing nodes; N_G represents the total grids or elements number; N represents the computing nodes used for the simulation; N_c represents the total cores used for the simulation; E_c represents the computational efficiency that is defined as the number of time units simulated per wall-clock hour; T_w represents the wall-clock time used for simulating 1000 time units. The data from OpenFOAM and Nektar++ in Table IX reflect their optimal computing configurations. Compared with them, the present CLBM model shows superior computational efficiency: 1.23 and 1.42 times greater when using 2 nodes, and 14.4 and 16.7 times greater when using 32 nodes. Considering the application of the uniform grids in the present simulations, the total grids number substantially surpasses those in OpenFOAM and Nektar++ models. Therefore, the efficiency gap is expected to expand with the incorporation of advanced grid techniques in the CLBM model.

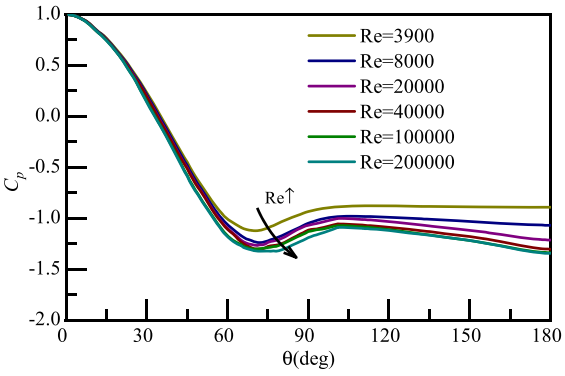

FIG. 20. Variation in the pressure coefficient along the cylinder surface for Re = 3900–2×10^5.

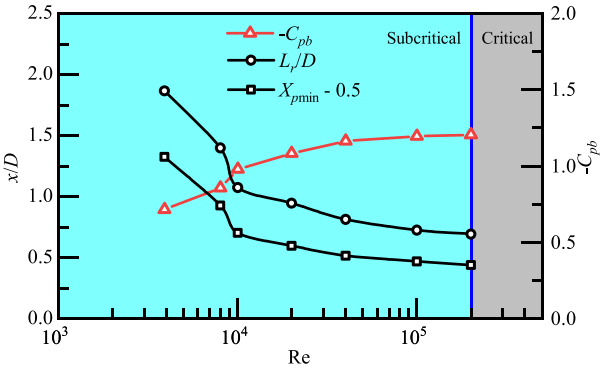

FIG. 21. The relationship between the low-pressure location and Re in the range of Re = 3900 to 2×10^5. The result is compared with the L_r – Re and $-C_{pb}$ – Re relationship.

The superiority of the present model also displays at the parallel scalability. As shown in Fig. 23, the speedup ratio and computational efficiency increase almost linearly with the addition of computing nodes in the present CLBM model. The OpenFOAM and Nektar++ models encounter scalability limits at 10 nodes and 2 nodes, respectively. This is attribute to the sharp rise in MPI communication time with using more nodes. Unlike these models, the CLBM model circumvents this issue through its inherently local and non-iterative nature, ensuring superior scalability.

VI. CONCLUSIONS

This paper focuses on the performance of the parameterized cumulant lattice Boltzmann method model for simulating flow past a circular cylinder within the subcritical Re range of 3900 to 2×10^5. The parameterized cumulant lattice Boltzmann model shows its ability in simulating the practical engineering flow with complex separation and recirculation. The following conclusions are drawn:

(1) The CLBM model demonstrates good agreement with experimental data and provides accurate flow field details on a relatively coarser grid resolution (up to $y^+ \approx 50$) when compared

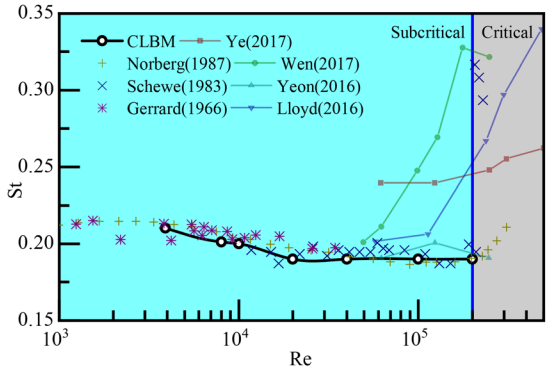

FIG. 22. The relationship between the St and Re in the range of Re = 3900 to 2×10^5. The scatters represent experimental data. The lines with solid symbol represent simulation results of other models. The line with hollow symbol represents the present CLBM results.

TABLE IX. Comparisons of the speedup ratio and computational efficiency using the reference case of Re = 3900 in Sec. III A. The OpenFOAM and Nektar++ data present in this table are the best performance case in Jiang and Cheng.[30]

Case	N_G ($\times 10^6$)	N (nodes)	N_c (cores)	Speedup ratio	E_c (time units/h)	T_w (h)
Case 4-1	179.84	1	56	1	1.33	752.77
Case 4-2	180.58	2	112	1.95	2.59	386.04
Case 4-3	182.07	4	224	3.72	4.94	202.35
Case 4-4	183.53	8	448	7.02	9.32	107.26
Case 4-5	187.31	16	896	12.63	16.78	59.61
Case 4-6	190.38	32	1792	22.88	30.39	32.91
OpenFOAM[30]	10.50	10	···	6.76	2.11	473.09
Nektar++[30]	0.42	2	···	1.55	1.82	550.78

with other numerical models ($y^+ = 0.03 - 2$). This advantage is attributed to the parameterized process, which increases the convergence order of the diffusion term. Furthermore, in contrast to other high-order FDM and HEM models, the fourth-order accuracy of the diffusion term is obtained on a completely local stencil by means of ghost cumulants in CLBM model. This feature maintains the excellent parallel scalability of the lattice Boltzmann method.

(2) The regularization process in the cumulant scheme serves two purposes. In addition to enhancing the stability in high Reynolds number simulations, it also dissipates high wave number energy. This process ensures the stability and accuracy of the cumulant lattice Boltzmann model in high Reynolds number simulations, even without explicit turbulence model. An analysis of the regularization parameter reveals that results converge when the grid resolution is sufficiently fine, while deviations in medium resolution are not substantial. The original form of the regularization is retained, and a slightly larger regularization parameter $\lambda = 0.1$ is recommended for flow past circular cylinder simulations at the subcritical range of Re = 3900 to 2×10^5. This recommendation strikes a balance between accuracy and computational cost, as achieving a sufficiently fine grid resolution at very high Reynolds numbers is often impractical. Although the heuristic work by Gehrke and Rung[67] suggested a resolution-sensitive regularization parameter, there is also a case-dependent factor needed to calibrate, from our perspective.

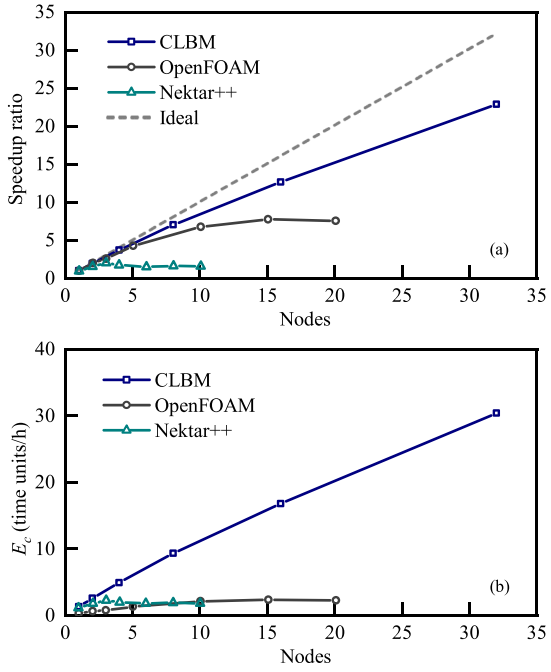

FIG. 23. Comparisons of the parallel scalability and computational efficiency: (a) speedup ratio and (b) computational efficiency, represented by the time units simulated in an hour wall-clock time.

(3) The flow properties and hydrodynamic forces variations in the subcritical range of Re = 3900 to 2×10^5 are thoroughly investigated through the present CLBM model. The key quantities like $\bar{C}_D$, C'_L, $-C_{pb}$ and St are achieving agreement with the experimental data. Through the near wake's instantaneous flow field, the present research provides qualitative insight into the physical mechanisms influencing these variations. Additionally, the present paper quantitatively demonstrates these mechanisms, highlighting the role of shear layer instability, recirculation region length, and low-pressure location movements in response to Reynolds number changes, thereby offering a comprehensive analysis of the flow dynamics involved. With the increasing instability in the shear layer, the turbulent transition point in the shear layers moves upstream which finally causes the recirculation region L_r decreases. When the L_r decreases, the low-pressure location also moves upstream. The variations of the $-C_{pb}$ and C'_L on Re are affected by the low-pressure location, thus showing inverse correlation with the $L_r - \mathrm{Re}$ relationship.

(4) The present CLBM model retains all the advantages of the LBM. The computational efficiency and parallel scalability are superior to the widely utilized models like OpenFOAM and Nektar++.

Finally, there are still some open issues that need further studies. Although the cumulant lattice Boltzmann model has excellent parallel scalability and good accuracy on a relatively coarser grid resolution (up to $y^+ \approx 50$), its application is still limited by the use of uniform and isotropic grids in the present study. The implementation of an

anisotropic grid and local grid refinement will be addressed in future research. Additionally, the present study only focuses on the flow past a circular cylinder, without considering the influence of the bottom bed. Future studies will explore flow around pile structures situated on a rigid bed, examining the combined effects of both the bottom bed and water depth.

ACKNOWLEDGMENTS

This study was financially supported by The National Key Research and Development Program of China (Grand No. 2021YFB2601100), the Joint Funds of the National Natural Science Foundation of China (Grant No. U1906231), and the National Natural Science Foundation of China (Grant Nos. 51979190 and 52301335).

AUTHOR DECLARATIONS

Conflict of Interest

The authors have no conflicts to disclose.

Author Contributions

Enbo Xing: Conceptualization (lead); Data curation (lead); Formal analysis (lead); Investigation (lead); Methodology (lead); Software (lead); Validation (lead); Visualization (lead); Writing – original draft (lead); Writing – review & editing (lead). **Guangwei Liu:** Conceptualization (supporting); Funding acquisition (supporting); Investigation (supporting); Methodology (supporting); Software (supporting); Supervision (supporting); Writing – review & editing (supporting). **Qinghe Zhang:** Data curation (supporting); Funding acquisition (lead); Methodology (supporting); Supervision (supporting); Writing – review & editing (supporting). **Jinfeng Zhang:** Funding acquisition (supporting); Resources (supporting); Supervision (supporting); Writing – review & editing (supporting). **Chaoqun Ji:** Formal analysis (supporting); Investigation (supporting); Methodology (supporting); Software (supporting).

DATA AVAILABILITY

The data that support the findings of this study are available from the corresponding author upon reasonable request.

REFERENCES

[1]J. F. Wilson, *Dynamics of Offshore Structures* (John Wiley & Sons, 2003).
[2]C. H. K. Williamson and R. Govardhan, "Vortex-induced vibrations," Annu. Rev. Fluid Mech. **36**, 413 (2004).
[3]D. Guan *et al.*, "Local scour at offshore windfarm monopile foundations: A review," Water Sci. Eng. **15**, 29 (2022).
[4]M. M. Zdravkovich, "Conceptual overview of laminar and turbulent flows past smooth and rough circular cylinders," J. Wind Eng. Ind. Aerodyn. **33**, 53 (1990).
[5]C. H. K. Williamson, "Vortex dynamics in the cylinder wake," Annu. Rev. Fluid Mech. **28**, 477 (1996).
[6]J. F. Derakhshandeh and M. M. Alam, "A review of bluff body wakes," Ocean Eng. **182**, 475 (2019).
[7]B. Forouzi Feshalami, S. He, F. Scarano, L. Gan, and C. Morton, "A review of experiments on stationary bluff body wakes," Phys. Fluids **34**, 011301 (2022).
[8]M. R. Lekkala *et al.*, "Recent advances in understanding the flow over bluff bodies with different geometries at moderate Reynolds numbers," Ocean Eng. **261**, 111611 (2022).
[9]B. Cantwell and D. Coles, "An experimental study of entrainment and transport in the turbulent near wake of a circular cylinder," J. Fluid Mech. **136**, 321 (1983).
[10]C. Norberg, "Effects of Reynolds number and a low-intensity freestream turbulence on the flow around a circular cylinder," Report No. 87/2 (Chalmers University of Technology, 1987).
[11]S. Szepessy and P. W. Bearman, "Aspect ratio and end plate effects on vortex shedding from a circular cylinder," J. Fluid Mech. **234**, 191 (1992).
[12]L. Ong and J. Wallace, "The velocity field of the turbulent very near wake of a circular cylinder," Exp. Fluids **20**, 441 (1996).
[13]J. H. Gerrard, "An experimental investigation of the oscillating lift and drag of a circular cylinder shedding turbulent vortices," J. Fluid Mech. **11**, 244 (1961).
[14]J. H. Gerrard, "The mechanics of the formation region of vortices behind bluff bodies," J. Fluid Mech. **25**, 401 (1966).
[15]J. S. Son and T. J. Hanratty, "Velocity gradients at the wall for flow around a cylinder at Reynolds numbers from 5×10^3 to 10^5," J. Fluid Mech. **35**, 353 (1969).
[16]M. J. Moeller, "Measurement of unsteady forces on a circular cylinder in cross flow at subcritical Reynolds numbers," Ph.D. thesis (Massachusetts Institute of Technology, 1983).
[17]G. Schewe, "On the force fluctuations acting on a circular cylinder in crossflow from subcritical up to transcritical Reynolds numbers," J. Fluid Mech. **133**, 265 (1983).
[18]C. Norberg and B. Sunden, "Turbulence and Reynolds number effects on the flow and fluid forces on a single cylinder in cross flow," J. Fluids Struct. **1**, 337 (1987).
[19]G. S. West and C. J. Apelt, "Measurements of fluctuating pressures and forces on a circular cylinder in the Reynolds number range 10^4 to 2.5×10^5," J. Fluids Struct. **7**, 227 (1993).
[20]C. Norberg, "An experimental investigation of the flow around a circular cylinder: Influence of aspect ratio," J. Fluid Mech. **258**, 287 (1994).
[21]C. Norberg, "LDV-measurements in the near wake of a circular cylinder," in *Proceedings of 1998 ASME Fluids Engineering Division, Advances in the Understanding of Bluff Body Wakes and Vortex-Induced Vibration* (American Society of Mechanical Engineers, 1998), Vol. 1281.
[22]J. De Wilde and R. Huijsmans, "Experiments for high Reynolds numbers VIV on risers," in*ISOPE International Ocean and Polar Engineering Conference* (ISOPE, 2001).
[23]S. Dong, G. E. Karniadakis, A. Ekmekci, and D. Rockwell, "A combined direct numerical simulation–particle image velocimetry study of the turbulent near wake," J. Fluid Mech. **569**, 185 (2006).
[24]P. Parnaudeau, J. Carlier, D. Heitz, and E. Lamballais, "Experimental and numerical studies of the flow over a circular cylinder at Reynolds number 3900," Phys. Fluids **20**, 085101 (2008).
[25]V. M. Molochnikov *et al.*, "SIV measurements of flow structure in the near wake of a circular cylinder at Re = 3900," Fluid Dyn. Res. **51**, 055505 (2019).
[26]A. Desai, S. Mittal, and S. Mittal, "Experimental investigation of vortex shedding past a circular cylinder in the high subcritical regime," Phys. Fluids **32**, 014105 (2020).
[27]S. M. Yeon, J. Yang, and F. Stern, "Large-eddy simulation of the flow past a circular cylinder at sub- to super-critical Reynolds numbers," Appl. Ocean Res. **59**, 663 (2016).
[28]W. Cheng, D. I. Pullin, R. Samtaney, W. Zhang, and W. Gao, "Large-eddy simulation of flow over a cylinder with from to: A skin-friction perspective," J. Fluid Mech. **820**, 121 (2017).
[29]G. Tian and Z. Xiao, "New insight on large-eddy simulation of flow past a circular cylinder at subcritical Reynolds number 3900," AIP Adv. **10**, 085321 (2020).
[30]H. Jiang and L. Cheng, "Large-eddy simulation of flow past a circular cylinder for Reynolds numbers 400 to 3900," Phys. Fluids **33**, 034119 (2021).
[31]D. A. Lysenko, I. S. Ertesvåg, and K. E. Rian, "Large-eddy simulation of the flow over a circular cylinder at Reynolds Number 2×10^4," Flow, Turbul. Combust. **92**, 673 (2013).
[32]R. M. Stringer, J. Zang, and A. J. Hillis, "Unsteady RANS computations of flow around a circular cylinder for a wide range of Reynolds numbers," Ocean Eng. **87**, 1 (2014).
[33]M. A. Prsic, M. C. Ong, B. Pettersen, and D. Myrhaug, "Large Eddy Simulations of flow around a smooth circular cylinder in a uniform current in the subcritical flow regime," Ocean Eng. **77**, 61 (2014).

[34]T. P. Lloyd and M. James, "Large eddy simulations of a circular cylinder at Reynolds numbers surrounding the drag crisis," Appl. Ocean Res. **59**, 676 (2016).
[35]H. Ye and D. Wan, "Benchmark computations for flows around a stationary cylinder with high Reynolds numbers by RANS-overset grid approach," Appl. Ocean Res. **65**, 315 (2017).
[36]P. Wen and W. Qiu, "Investigation of drag crisis phenomenon using CFD methods," Appl. Ocean Res. **67**, 306 (2017).
[37]W. Qiu *et al.*, "Numerical benchmark studies on drag and lift coefficients of a marine riser at high Reynolds numbers," Appl. Ocean Res. **69**, 245 (2017).
[38]F. S. Pereira, L. Eça, G. Vaz, and S. S. Girimaji, "On the simulation of the flow around a circular cylinder at Re = 140,000," Int. J. Heat Fluid Flow **76**, 40 (2019).
[39]B. F. Garcia, G. D. Weymouth, V.-T. Nguyen, and O. R. Tutty, "Span effect on the turbulence nature of flow past a circular cylinder," J. Fluid Mech. **878**, 306 (2019).
[40]H. Jiang, "Separation angle for flow past a circular cylinder in the subcritical regime," Phys. Fluids **32**, 014106 (2020).
[41]G. Fan, Y. Liu, W. Zhao, and D. Wan, "Effect of wall stress models and subgrid-scale models for flow past a cylinder at Reynolds number 3900," Phys. Fluids **36**, 015152 (2024).
[42]A. G. Kravchenko and P. Moin, "Numerical studies of flow over a circular cylinder at Re_D=3900," Phys. Fluids **12**, 403 (2000).
[43]W. Sarwar and F. Mellibovsky, "Characterization of three-dimensional vortical structures in the wake past a circular cylinder in the transitional regime," Phys. Fluids **32**, 074104 (2020).
[44]M. Faizal Ahmad, M. R. Mohd Haniffah, A. Kueh, and E. H. Kasiman, "Numerical study on drag and lift coefficients of a marine riser at high Reynolds number using COMSOL multiphysics," IOP Conf. Ser.: Earth Environ. Sci. **476**, 012075 (2020).
[45]G. Liu, J. Zhang, and Q. Zhang, "A high-performance three-dimensional lattice Boltzmann solver for water waves with free surface capturing," Coastal Eng. **165**, 103865 (2021).
[46]E. Xing, Q. Zhang, G. Liu, J. Zhang, and C. Ji, "A three-dimensional model of wave interactions with permeable structures using the lattice Boltzmann method," Appl. Math. Modell. **104**, 67 (2022).
[47]S. Watanabe and T. Aoki, "Large-scale flow simulations using lattice Boltzmann method with AMR following free-surface on multiple GPUs," Comput. Phys. Commun. **264**, 107871 (2021).
[48]M. Bauer *et al.*, "waLBerla: A block-structured high-performance framework for multiphysics simulations," Comput. Math. Appl. **81**, 478 (2021).
[49]J. Latt *et al.*, "Palabos: Parallel lattice Boltzmann Solver," Comput. Math. Appl. **81**, 334 (2021).
[50]M. Geier, M. Schönherr, A. Pasquali, and M. Krafczyk, "The cumulant lattice Boltzmann equation in three dimensions: Theory and validation," Comput. Math. Appl. **70**, 507 (2015).
[51]M. Geier, A. Pasquali, and M. Schönherr, "Parametrization of the cumulant lattice Boltzmann method for fourth order accurate diffusion part I: Derivation and validation," J. Comput. Phys. **348**, 862 (2017).
[52]D. D'Humières, I. Ginzburg, M. Krafczyk, P. Lallemand, and L. S. Luo, "Multiple-relaxation-time lattice Boltzmann models in three dimensions," Philos. Trans. R. Soc. A **360**, 437 (2002).
[53]R. Du, B. Shi, and X. Chen, "Multi-relaxation-time lattice Boltzmann model for incompressible flow," Phys. Lett. A **359**, 564 (2006).
[54]K. Suga, Y. Kuwata, K. Takashima, and R. Chikasue, "A D3Q27 multiple-relaxation-time lattice Boltzmann method for turbulent flows," Comput. Math. Appl. **69**, 518 (2015).
[55]M. Geier, A. Greiner, and J. G. Korvink, "Cascaded digital lattice Boltzmann automata for high Reynolds number flow," Phys. Rev. E **73**, 066705 (2006).
[56]P. Asinari, "Generalized local equilibrium in the cascaded lattice Boltzmann method," Phys. Rev. E **78**, 016701 (2008).
[57]A. De Rosis, "Non-orthogonal central moments relaxing to a discrete equilibrium: A D2Q9 lattice Boltzmann model," Europhys. Lett. **116**, 44003 (2017).
[58]A. De Rosis, "Nonorthogonal central-moments-based lattice Boltzmann scheme in three dimensions," Phys. Rev. E **95**, 013310 (2017).
[59]S. Ansumali and I. V. Karlin, "Single relaxation time model for entropic lattice Boltzmann methods," Phys. Rev. E **65**, 056312 (2002).
[60]F. Bosch, S. S. Chikatamarla, and I. V. Karlin, "Entropic multirelaxation lattice Boltzmann models for turbulent flows," Phys. Rev. E **92**, 043309 (2015).
[61]M. Geier, A. Pasquali, and M. Schönherr, "Parametrization of the cumulant lattice Boltzmann method for fourth order accurate diffusion part II: Application to flow around a sphere at drag crisis," J. Comput. Phys. **348**, 889 (2017).
[62]S. Lenz *et al.*, "Towards real-time simulation of turbulent air flow over a resolved urban canopy using the cumulant lattice Boltzmann method on a GPGPU," J. Wind Eng. Ind. Aerodyn. **189**, 151 (2019).
[63]H. Asmuth, H. Olivares-Espinosa, and S. Ivanell, "Actuator line simulations of wind turbine wakes using the lattice Boltzmann method," Wind Energy Sci. **5**, 623 (2020).
[64]C. Feuchter, "Direct aeroacoustic simulation with a cumulant Lattice-Boltzmann model," Comput. Fluids **224**, 104970 (2021).
[65]M. Geier, S. Lenz, M. Schönherr, and M. Krafczyk, "Under-resolved and large eddy simulations of a decaying Taylor–Green vortex with the cumulant lattice Boltzmann method," Theor. Comput. Fluid Dyn. **35**, 169 (2020).
[66]A. Pasquali, M. Geier, and M. Krafczyk, "Near-wall treatment for the simulation of turbulent flow by the cumulant lattice Boltzmann method," Comput. Math. Appl. **79**, 195 (2020).
[67]M. Gehrke and T. Rung, "Scale-resolving turbulent channel flow simulations using a dynamic cumulant lattice Boltzmann method," Phys. Fluids **34**, 075129 (2022).
[68]M. Gehrke and T. Rung, "Periodic hill flow simulations with a parameterized cumulant lattice Boltzmann method," Int. J. Numer. Methods Fluids **94**, 1111 (2022).
[69]X. He and L. S. Luo, "Lattice Boltzmann model for the incompressible Navier–Stokes equation," J. Stat. Phys. **88**, 927 (1997).
[70]S. Izquierdo and N. Fueyo, "Characteristic nonreflecting boundary conditions for open boundaries in lattice Boltzmann methods," Phys. Rev. E **78**, 046707 (2008).
[71]M. B. Schlaffer, *Non-Reflecting Boundary Conditions for the Lattice Boltzmann Method* (Technische Universität München, 2013).
[72]D. Heubes, A. Bartel, and M. Ehrhardt, "Characteristic boundary conditions in the lattice Boltzmann method for fluid and gas dynamics," J. Comput. Appl. Math. **262**, 51 (2014).
[73]D. Yu, R. Mei, and W. Shyy, "A unified boundary treatment in lattice Boltzmann method," AIAA Paper No. 2003-953, 2003.
[74]Z. Guo, C. Zheng, and B. Shi, "An extrapolation method for boundary conditions in lattice Boltzmann method," Phys. Fluids **14**, 2007 (2002).
[75]P. Beaudan and P. Moin, "Numerical experiments on the flow past a circular cylinder at sub-critical Reynolds number," Report No. TF-62 (Stanford University, 1995).
[76]M. Gehrke, A. Banari, and T. Rung, "Performance of under-resolved, model-free LBM simulations in turbulent shear flows," in *Progress in Hybrid RANS-LES Modelling*(Springer, 2020), p. 3.
[77]R. T. Keefe, "Investigation of the fluctuating forces acting on a stationary circular cylinder in a subsonic stream and of the associated sound field," J. Acoust. Soc. Am. **34**, 1711 (1962).
[78]B. Stahl, B. Chopard, and J. Latt, "Measurements of wall shear stress with the lattice Boltzmann method and staircase approximation of boundaries," Comput. Fluids **39**, 1625 (2010).